

36 and contribution to sea level, especially given that more of these extremes are predicted under a
37 warmer climate.

38 **Keywords:** Ice shelf calving, icebergs, Amery Ice Shelf, East Antarctica, blocking highs, polar
39 cyclones, explosive cyclones.

40 **1. Introduction**

41 The rapid collapse of several Antarctic ice shelves, observed recently, and the near-instantaneous
42 acceleration of land-ice discharge into the ocean that follows the collapse, demonstrates the
43 sensitivity of the Antarctic cryosphere to recent warming (e.g., Smith et al., 2019; Rignot et al.,
44 2019). However, large uncertainty remains regarding the response of ice shelves to the globally
45 rising temperatures and to the resulting changes in the atmospheric circulation.

46 On 25 September 2019, the Amery Ice Shelf – the third largest ice shelf in Antarctica – calved
47 iceberg D28 (1,636 km², 210 m thick), which was the largest calving event since the early 1960s
48 (Fig. 1). The Amery Ice Shelf is a key drainage channel in East Antarctica (Fricker et al., 2002)
49 draining roughly 16% of the East Antarctic Ice Sheet (Galton-Fenzi et al., 2012). It is in balance
50 with its surroundings (King et al., 2009; Galton-Fenzi et al., 2012; Li et al., 2020), despite
51 experiencing strong surface melt in summer. However, over the past 20 years, a large system of
52 rifts (a precursor to calving) in the Amery Ice Shelf, known as the Loose Tooth rift system, has
53 been developing (Fricker et al., 2005; Bassis et al., 2008; Darji et al., 2018). Recent studies have
54 shown that the propagation rate of the rifts has been decreasing since 2005 due to increasing
55 thickness of mélange ice filling in the rifts, and speculated that forward propagation of the west
56 rift might even stop (e.g., Zhao et al., 2013). Satellite images of the Amery Ice Shelf (Fig. 1) show
57 the largest rift extending in the same direction of the ice flow, widening toward the edge of the ice
58 shelf and from this main rift, with radial rifts extending to the west (T1) and east (T2). Earlier
59 studies predicted that the Amery Ice Shelf would not experience a major calving until around 2025
60 or later. (e.g., Fricker et al., 2002), and the portion that was expected to calve first was T2 i.e., the
61 one to the east of the current calving. This highlights the need for an improved understanding of
62 the underlying processes of calving events and the role of atmospheric forcing as trigger for ice
63 shelf calving.

64 Indeed, most of the mass loss from the Antarctic Ice Sheet – the largest uncertainty for future sea
65 level projections – takes place at the fronts of ice shelves and glacier tongues, via iceberg calving
66 and surface and basal melt (e.g., Pritchard et al., 2012; Shepherd et al., 2018). Compared to
67 melting, rifting and subsequent calving is the fastest way by which marine-terminating glaciers
68 lose mass to the ocean and contribute therefore to sea level rise (e.g., Smith et al., 2019). Despite
69 being floating ice (i.e., changes in their mass due to calving do not have a direct contribution to
70 sea level rise), ice shelves in general act to buttress inland ice by blocking the flow of ice from the
71 interior (Scambos et al., 2008). This restrictive force decreases when ice shelves thin or calve. For
72 example, on the Antarctic Peninsula, such events have been shown to increase by eight-fold the
73 rate of ice flow inland (Rignot et al., 2004; Scambos et al., 2004; 2014). This leads to more ice
74 discharge into the oceans and a consequent increase in the ice-sheet contribution to global sea-
75 level rise (Hogg and Gudmundsson, 2017). Ocean-driven thinning was also detected at key ice

76 shelves of the East Antarctic Ice Sheet including the Amery Ice Shelf (Greenbaum et al., 2015;
77 Smith et al., 2019) suggesting that this region is also susceptible to rapid and large-scale ice loss
78 (Aitken et al., 2016), and could contribute to future sea-level rise (DeConto et al., 2016; Rignot et
79 al., 2019). Therefore, there is a need to assess the sensitivity of East Antarctic ice shelves to
80 atmospheric forcing and to understand the calving processes and their triggers in order to be able
81 to model the future evolution of ice shelves.

82 Beyond being part of a natural glaciological process, calving events at Antarctic ice shelves have
83 been attracting much attention recently (e.g., Liu et al., 2015; Benn and Astrom 2018) as they were
84 found to trigger, in some cases, the total disintegration of the parent ice shelf (Cook and Vaughan
85 2010; Liu et al., 2015; Jeong et al., 2016; Bassis and Ma, 2016; Massom et al., 2018). These events
86 have been attributed mainly to an enhanced regional warming (Vaughan et al., 2012; Pitchard et
87 al. 2012) which increases surface and basal melt as well as to ocean forcing involving intense
88 crevassing and rifting along multiple lines of weakness such as radial crevasses (Liu et al., 2015;
89 Jeong et al., 2016; Bassis and Ma, 2016), to earthquake and tsunami (Brunt et al., 2011) and to
90 regional loss of pack ice in the shelf-front area which allows storm-generated ocean swell to flex
91 the outer margins of the shelves and lead to their calving (Massom et al., 2018). However,
92 atmospheric-dynamics forcing during calving events, particularly the wind mechanical action on
93 rift widening via wind-induced tides and ocean slope, remains unexplored and this the objective
94 of this study.

95 Of particular importance is the impact on Antarctic ice shelves of the poleward shift of
96 extratropical storm tracks (Tamarin and Kaspi, 2017) and the observed increase in the number and
97 intensity of cyclones around Antarctica over the last few decades (Rudeva et al., 2015; Wei and
98 Qin 2016). The poleward shift of extratropical cyclones was found in reanalysis data of recent
99 years (Fyfe, 2003; Son et al., 2008), and models (e.g., Neu et al., 2013) project an estimated
100 poleward shift of cyclone genesis 1° to 2° in latitude on average under enhanced greenhouse gas
101 concentrations (Bengtsson et al., 2009; Barnes and Polvani, 2013). Importantly, this poleward shift
102 was found to be particularly pronounced in the Southern Hemisphere (Pezza et al., 2007; Chang
103 et al., 2012), and the mean intensity of cyclones as well as the number of extreme cyclones are
104 projected to increase under a warmer climate scenario (Lambert and Fyfe, 2006; Ulbrich et al.,
105 2013; Chang, 2017).

106 Changes in cyclone tracks, numbers, and intensity may have significant impacts on Antarctic sea
107 ice and land ice (e.g., Uotila et al., 2011). In fact, weather systems (i.e., cyclones and blocks)
108 resulting from the larger-scale circulation (e.g., Pope et al., 2017) are identified as the main driver
109 of the observed trends in sea ice variability (Matear et al., 2015; Schemm, 2018; Turner et al.,
110 2017; Eayrs et al., 2019). Furthermore, cyclones and their associated atmospheric rivers can induce
111 sea ice melt (Francis et al., 2020) and ice-shelf surface melt (Wille et al., 2019) by virtue of their
112 associated anomalous moisture and heat transport to high latitudes which increase the downward
113 longwave radiation at the ice surface (Woods & Caballero, 2016; Lee et al., 2017; Grieger et al.,
114 2018; Francis et al., 2020). Additionally, cyclones can cause significant sea ice drift (Kwok et al.,
115 2017; Francis et al., 2019a) due to the strong surface winds they carry (Schemm, 2018). Severe
116 storms can generate energetic waves (up to 8 m) in the Southern Ocean capable of penetrating

117 hundreds of kilometers into the sea ice covered ocean (Kohout et al., 2014; Vichi et al., 2019;
118 Squire, 2020) Concomitantly, the sea ice cover acts as a buffer and attenuates the wave energy
119 over distance (wave amplitude is reduced by several orders of magnitude within 10km of the sea
120 ice edge), reducing therefore the impact of storms on ice shelves (Dolatshah et al., 2018; Massom
121 et al., 2018).

122 An extreme situation in cyclogenesis is the formation of explosive cyclones. These are developing
123 cyclones for which the central pressure decreases by at least 24 hPa in 24 hours (Sanders and
124 Gyakum, 1980). Explosively developing cyclones are deeper and longer-lasting compared to
125 ordinary cyclones and they are found to be more intense in the Southern Hemisphere than in the
126 Northern Hemisphere (Raele et al., 2019). In particular, explosive cyclones in the Indian Ocean
127 sector of the Southern Ocean (close to South Africa) are stronger and express higher deepening
128 rates than elsewhere around Antarctica (Raele et al., 2019). This same region (between 45°E and
129 90°E and poleward of 40°S) – encompassing the Amery Basin – stands out in a climatological
130 study (Allen et al., 2010) as one of three main regions for explosive cyclogenesis around
131 Antarctica, where explosive cyclones are characterized by a 20hPa mean pressure depth relative
132 to the surrounding pressure field. A climatological study of explosive cyclones (Lim and
133 Simmonds, 2002) found that the number of explosive cyclones increased in both hemispheres
134 during 1979-1999, and that positive trends of such systems are statistically significant in the
135 Southern Hemisphere. On average, the study identified 26 explosive cyclones per year in the
136 Southern Hemisphere and found that explosive cyclones exhibit greater mean intensity and depth
137 relative to the entire population of ordinary cyclonic systems. A more recent climatological study
138 over a longer period (1979–2013) reported similar findings, with an increase in the frequency of
139 explosive cyclones in the band of 45°–55°S during winter and early spring (Wei and Qin 2016).

140 The spatial distribution of these cyclones was found to have a close association with that of strong
141 baroclinicity. In general, the preferred region for cyclogenesis is where both a strong temperature
142 gradient and an upper-level trough are present (e.g., Shimada et al., 2014). While high baroclinic
143 instability associated with the horizontal temperature gradient is crucial for the formation and the
144 intensification of cyclones (Davies, 1997, Uccellini, 1990), cyclogenesis occurs only at the
145 entrance and exit regions of upper-level troughs (e.g., Shimada et al., 2014). Around Antarctica,
146 the strongest temperature gradient is found during late winter-early spring along the fringes of the
147 ice pack, making the sea-ice edge a preferred region for cyclogenesis (e.g., Schlosser et al., 2011;
148 Stoll et al., 2018). However, the location of the temperature gradient relative to the ice edge
149 depends strongly on the atmospheric circulation at larger scale, where a strong temperature
150 gradient can occur poleward of the ice edge (i.e., closer to the ice shelves) during an enhanced
151 zonal wave number three (ZW3) pattern (Irving and Simmonds, 2015). This pattern is
152 characterized by the alternation of 3 troughs and 3 ridges around Antarctica. Strong poleward
153 transport of heat and moisture occurs in the ascending branch of troughs and strong equatorward
154 transport of cold air occurs in the descending branch of ridges (e.g., Raphael, 2007). This zonally-
155 alternating pattern of cold and warm air masses creates temperature differences between the
156 different sectors, fuels frontogenesis and promotes the development of explosive cyclones close to
157 the ice shelves and over the sea ice cover.

158 Another aspect of the ZW3 pattern is the impact of the ridges on the propagation speed of the
159 cyclones. In the troughs, the extratropical cyclones and the associated moisture and heat fluxes are
160 directed poleward; once they reach the Antarctic coast they are blocked by the ridges to their east
161 (Francis et al., 2019a; 2020). This results in stationary cyclones over the same region for 1-2 days
162 which in turn induces pronounced impact on the sea ice (e.g., Francis et al., 2019a) and waves
163 (Vichi et al., 2019). The same scenario can happen at the front of ice shelves during winter-spring
164 if the cyclones form closer to the coast and/or the sea ice extent decreases under a warmer climate.
165 Interestingly, the Antarctic sea ice extent has been decreasing since 2015 (Swart et al., 2018) and
166 the ZW3 index has been the most positive on record during the same period (Schlosser et al., 2018;
167 Francis et al., 2019a). Increased warm air advection toward Antarctica was found to be at the origin
168 of the observed negative anomaly in Antarctic sea ice extent in recent years (Schlosser et al., 2018).
169 Given the dual impact of ZW3 circulation on both explosive cyclogenesis (location and intensity)
170 and sea ice extent, this combination may result in a more pronounced impact of extreme cyclones
171 on ice shelves.

172 Another extreme situation in cyclogenesis is the formation of twin cyclones during which the
173 resulting effect of the mutually-interacting cyclones is twice as strong as the individual cyclones
174 (e.g., Moustououi et al., 2002). To our knowledge, the formation of explosively developing twin
175 cyclones has been, to date, only observed and studied in the tropics (Ferreira et al., 1996;
176 Moustououi et al., 2002), in the mid-latitudes (Yokoyama and Yamamoto, 2019) and in the Arctic
177 (Renfrew et al., 1997). In this study, we report for the time, the formation of polar twin cyclones
178 near Antarctica during two consecutive events; one on 19-20 September 2019 at 60°E and the
179 second on 23-24 September 2019 at 85°E.

180 Despite the observed poleward shift of extratropical cyclones, the increasing number and intensity
181 of explosive cyclones around Antarctica and the decline in sea ice extent in recent years, the impact
182 of extreme cyclones on ice shelves instability has not been investigated to date.

183 Building on previous studies that investigated these patterns separately, we aim in this study to
184 assess the impact of extreme cyclone activity during the largest calving event since 1963 at the
185 Amery Ice Shelf. Using satellite data and atmospheric reanalyses, we investigate the role of
186 atmospheric forcings in this calving event which occurred under a ZW3-like situation. The
187 development of the explosive cyclones and their impact on sea ice and land ice conditions are
188 addressed in section 2. Section 3 discusses our findings. The data and methods used in this study
189 are described in section 4.

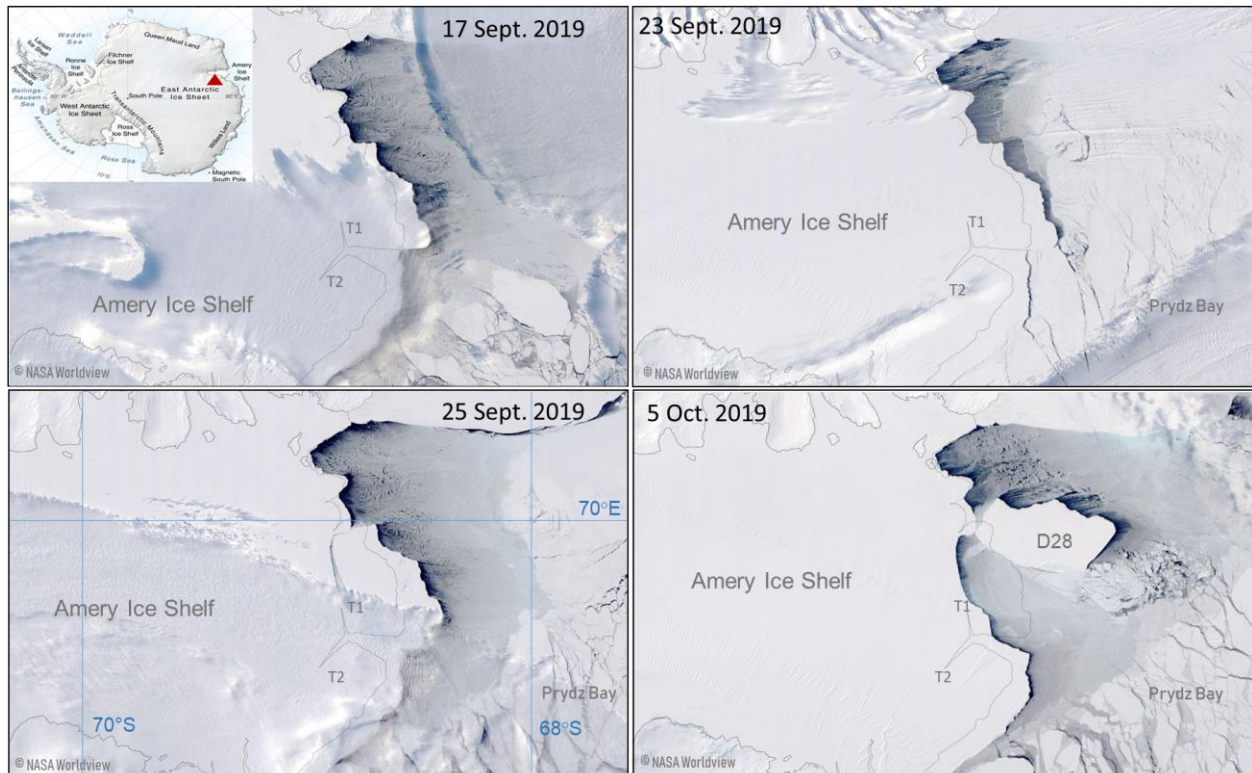


Figure 1: MODIS satellite visible imagery of the Amery Ice Shelf and the Loose Tooth rift system (T1 and T2) at its front. Ice conditions are shown before the calving on 17 and 23 September 2019, during the calving on 25 September 2019, and few days after the detachment of the new iceberg D28. Image credit NASA Worldview.

190

191 2. Results

192 2.1 Explosive twin cyclones during 18-22 September 2019 – preconditioning

193 In September 2019, the synoptic conditions exhibited an amplified zonal wave number 3 (ZW3)
 194 pattern characterized by 3 trough/ridge systems associated with low/high mean sea level pressure
 195 (MSLP) anomalies. Compared to all Septembers in the 1979-2019 period, the broad scale MSLP
 196 anomaly indicates that, for September 2019, there was below average pressure over much of the
 197 Antarctic continent and above average pressure to the north (Fig. 2a). In the Indian Ocean sector,
 198 the MSLP anomalies exceeded one standard deviation from the mean over large areas with the
 199 strongest troughing over Cooperation and Davis Seas (Fig. 2a). To the west of this low pressure
 200 anomaly, the South Atlantic ridge exhibited strong positive anomalies exceeding 2 standard
 201 deviations from the mean (Fig. 2a). To the east of the low pressure anomaly around the Amery Ice
 202 Shelf, another pronounced ridge encompassing south Australia and the Mawson Sea with positive
 203 MSLP anomalies exceeded 1 standard deviation from the climatological mean (Fig. 2a).

204 On a daily scale, the aforementioned synoptic setting was synonym of frequent and extreme
 205 weather systems. On 17 September 2019 at 0200 UTC, an extratropical cyclone associated with a
 206 968 hPa low-pressure at its center and located at 60°S, 40°E, started to deepen while moving
 207 poleward and eastward. It reached the western side of Cooperation Sea on 18 September 2019 at

208 0200 UTC with a 940 hPa minimum pressure and remained over this region the entire day (Fig.
 209 2b), then decayed on 19 September, with 980 hPa central pressure by 1300 UTC. The rapid
 210 deepening of the low pressure is characteristic of explosive cyclones (e.g., Sanders and Gyakum,
 211 1980). The explosive cyclone on 18 September 2019 was associated with significant poleward
 212 transport of moisture (Fig. 2c) and heat (Fig. 2d) carried by an atmospheric river propagating
 213 poleward adjacent to the low-pressure center. The atmospheric river was associated with integrated
 214 water vapor transport (IVT) greater than $500 \text{ kg m}^{-1} \text{ s}^{-1}$ at its core, with IVT values around 100 kg
 215 $\text{m}^{-1} \text{ s}^{-1}$ over Prydz Bay exceeding the 99th percentile of September climatology in this region (Fig.
 216 3a). The moisture and heat carried by the atmospheric river over the ice sheet may have caused
 217 warming at the surface due to condensation (released heat) as well as by increase in downward
 218 longwave radiation (e.g., Francis et al., 2020).

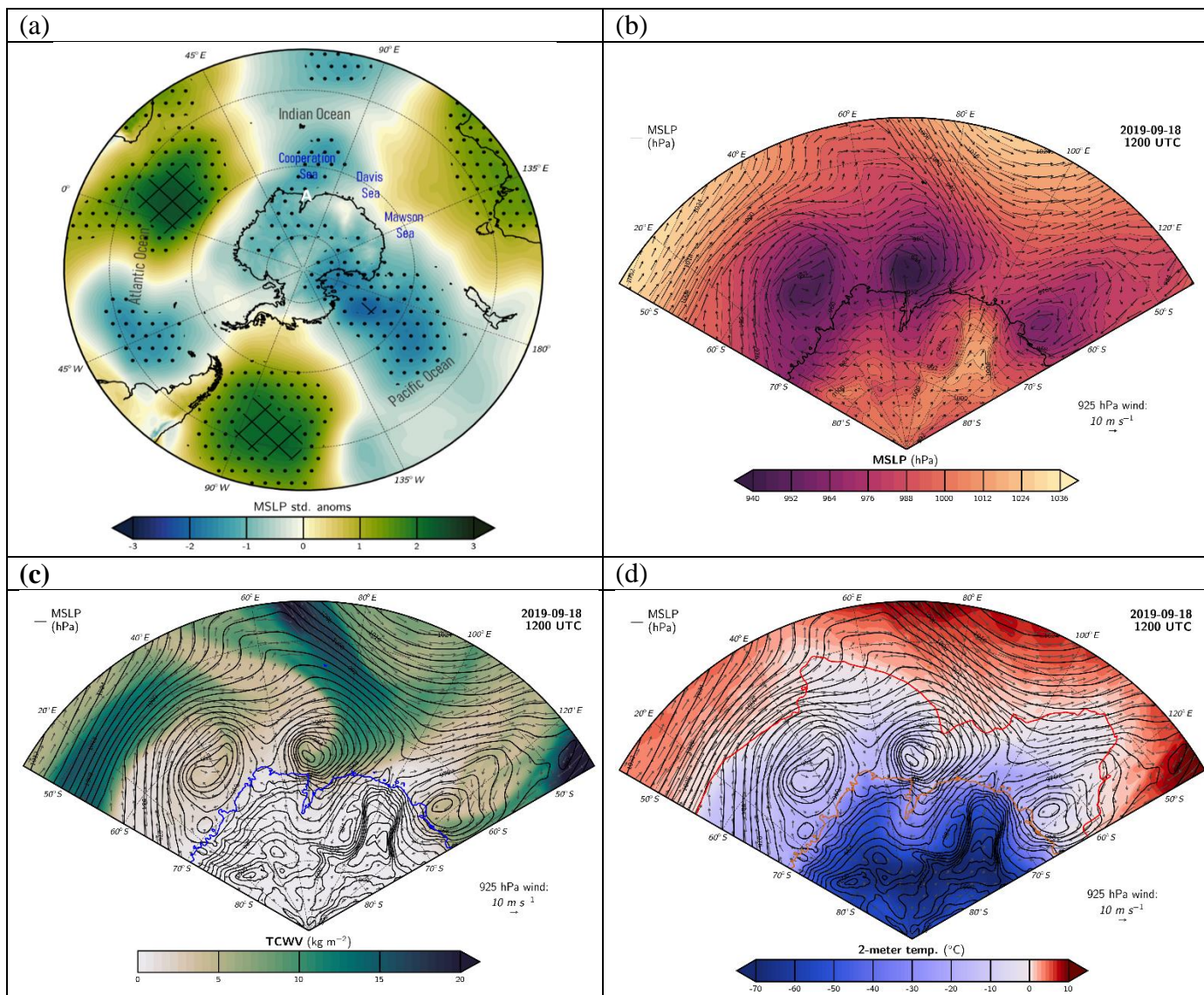


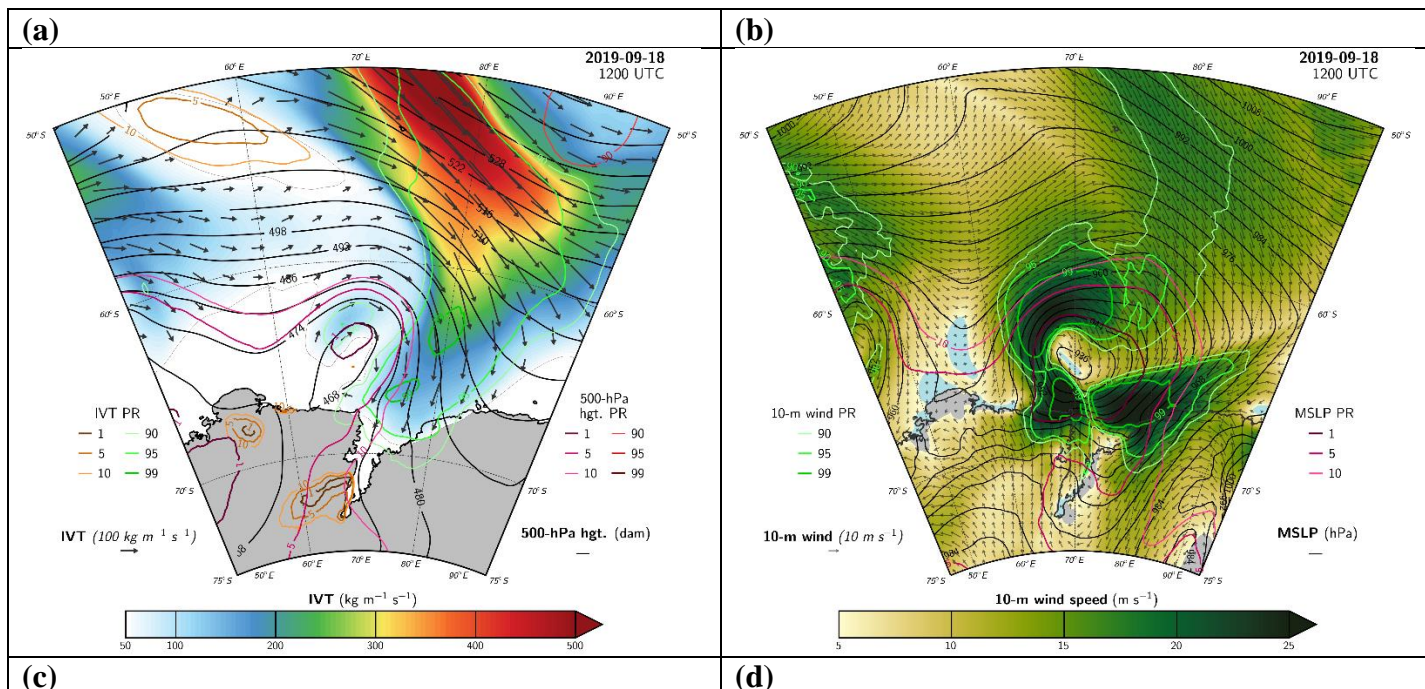
Figure 2: Normalized anomalies of Mean Sea Level Pressure (MSLP) for September 2019 relative to the 1979-2019 September climatology. Black dots are regions where the normalized anomalies are larger than 1 standard deviation from the mean and black squares are regions where the normalized anomalies are

larger than 2 standard deviations from the mean. The letter A in white indicates the location of the Amery Ice Shelf. (b) MSLP (shaded) and winds at 925hPa (vectors) at 18 September 2019 1200 UTC, (c) same as (b) but for the total column water vapor (TCWV) in colors, winds at 925hPa in vectors and MSLP in black contours, (d) same as (c) but for 2-m temperature (in colors), winds at 925hPa in vectors, MSLP in black contours and 0°C contour in red.

219

220 In the Southern Hemisphere, where cyclonic winds spin clockwise, the highest wind speed occurs
 221 along the bent-back front of the cyclone, i.e., to the west of the low-pressure center of the cyclone
 222 (e.g., Wagner et al., 2011, Watanabe and Niino, 2014). This was observed during the explosive
 223 cyclone on 18 September 2019 which generated extremely strong surface winds to the west of its
 224 center exceeding 20 m s^{-1} (Fig. 3b). Being stationary over Cooperation Sea but to the west of the
 225 Amery Basin, this extreme cyclone generated a sustained northeasterly wind stress over the
 226 northern part of the ice shelf (Fig. 3b), as well as strong poleward warm and moist air advection
 227 (Fig. 2c, 2d and 3a). The combination of warm temperatures brought by the cyclone/AR and strong
 228 easterly/northeasterly wind speeds was unusual (Fig. 3). MSLP anomalies during this event were
 229 in excess of -4 standard deviations (Fig. 3b), with MSLP values below the 1st percentile of
 230 September climatology over a large area along and to the north of the ice shelf margin (Fig. 3b).
 231 Extreme wind anomalies exceeding the 99th percentile over the central and eastern ice shelf margin
 232 were associated with this cyclone from 18 September through 19 September 2019 (Fig. 3c).
 233 Surface winds of 25 m s^{-1} , relative to 99 percentiles (5 standard deviations above the climatological
 234 mean), were registered during this event (Fig. 3b and 3c). Likewise, there were sustained positive
 235 2-m temperature anomalies throughout the period exceeding 2 standard deviations from the
 236 climatological mean (Fig. 3d).

237



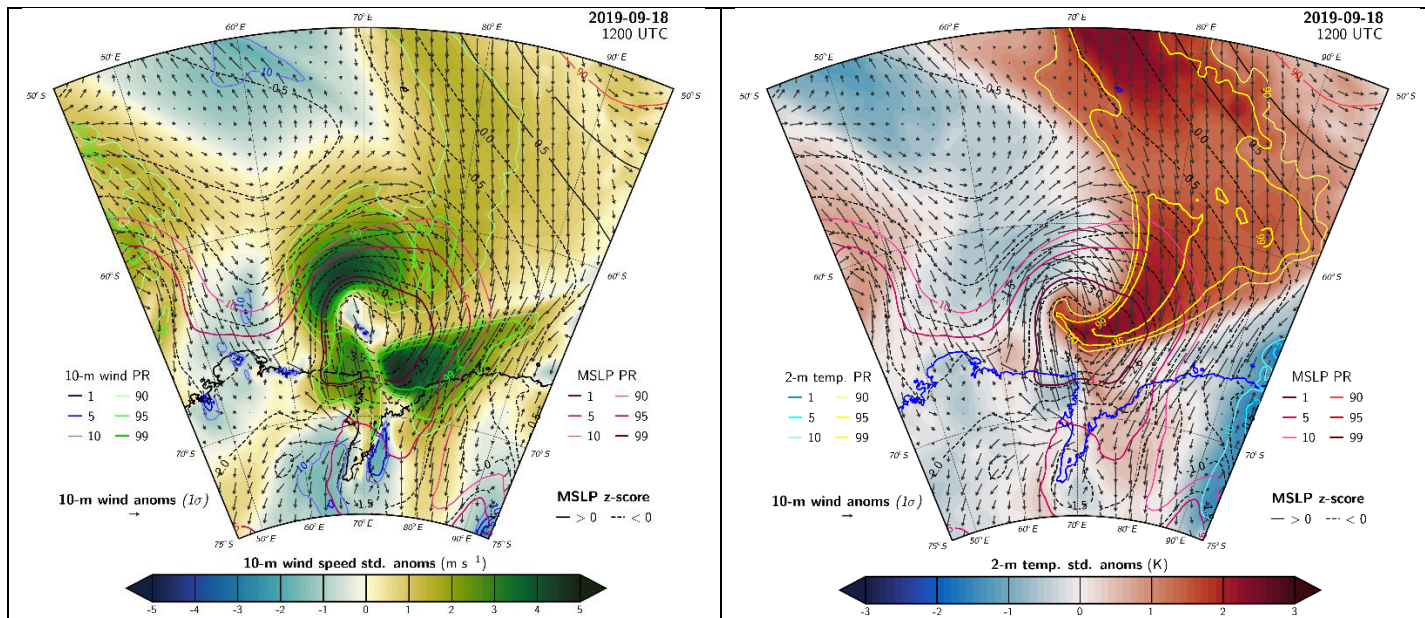


Figure 3: Maps on 18 September 2019 at 1200 UTC of (a) Integrated water vapor transport (IVT) shaded, geopotential heights at 500 hPa in black contours and IVT direction in black vectors, (b) 10-m wind speed in colors, 10-m wind direction in black vectors and MSLP in black contours. (c) Standardized 10-m wind speed anomalies relative to the full September record (1979-2019) (d) Same as (c) but for 2-m temperature. Colored contour lines show percentile rank extremes (1, 5, 10 and 90, 95, 99 percentile ranks) of the corresponding quantities indicated on the plots. On (c) and (d): Vectors show 10-m wind anomalies, black contours show positive MSLP anomalies and dashed black contours show negative MSLP anomalies.

238

239 The first explosive cyclone on 18 September 2019 was followed immediately by a second
 240 explosive cyclone which approached Cooperation Sea from the west on 19 September at 1400
 241 UTC with a deep low of 952hPa. At 2000UTC, this deep cyclone widened and evolved into two
 242 twin polar cyclones over the same region (Fig. 4a). The twin cyclones exhibited 960hPa low-
 243 pressure at their respective centers and remained active to the west of the Amery Ice Shelf for three
 244 consecutive days (Fig. 4a). Their signatures dissipated in the pressure field on 22 September 2019
 245 at 0000UTC. The poleward transport of heat (Fig. 4b) and moisture (Fig. 4c) towards the Amery
 246 Ice Shelf continued during this event together with extreme wind stress exceeding the 99th
 247 percentile (Fig. 4d). Being stationary to the west of the Amery Ice Shelf (Fig. 4a), the twin cyclones
 248 induced extreme easterly winds across the ice shelf, with u-wind anomalies exceeding -5 standard
 249 deviations of September climatology over the western ice shelf from 19 September 2019 at 1900
 250 UTC through 20 September at 1100 UTC (Fig. 4d) and below the 1 percentile u-wind values over
 251 the whole lower ice shelf area (Fig. 4d). When compared with the climatology for all months
 252 during 1979-2019, many hourly wind speeds over the ice shelf front during 18-20 September were
 253 substantially greater than the 99th percentile of climatology, with the most anomalous wind speeds
 254 on 18 September (Fig. 6e).

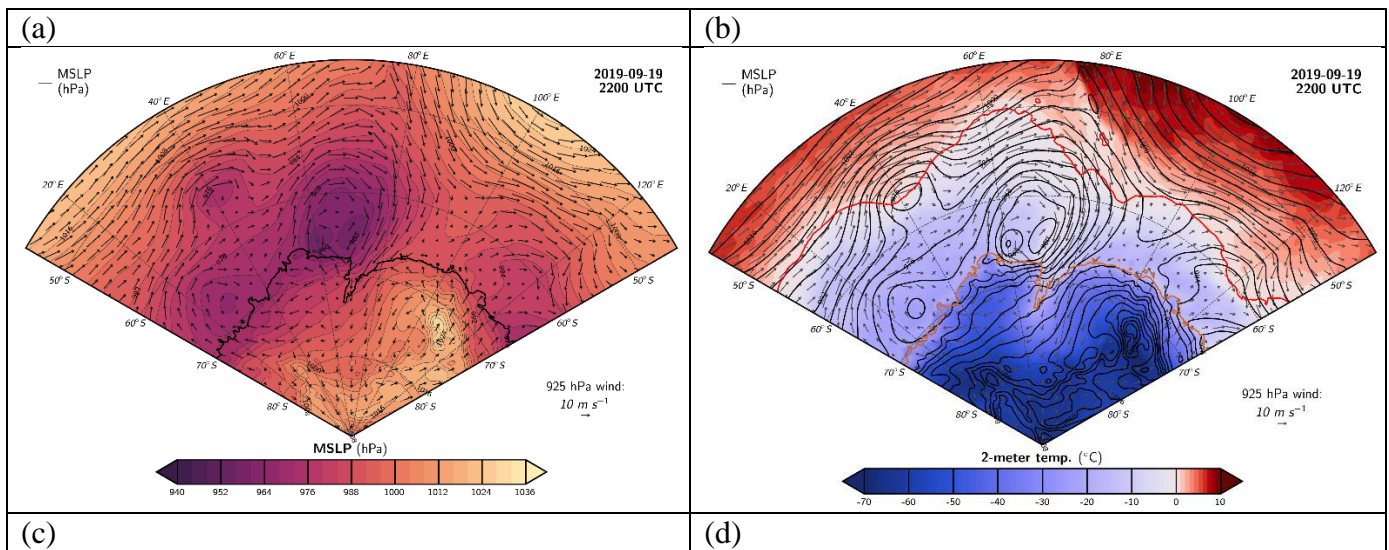
255 On 21 September 2019, the twin cyclones merged and moved to the area in front of the Amery Ice
 256 Shelf (Fig. 4e) resulting in a deep cyclone associated with MSLP at its center below the 5th
 257 percentile. The remnant cyclone slowly moved along the northern margin of Prydz Bay and

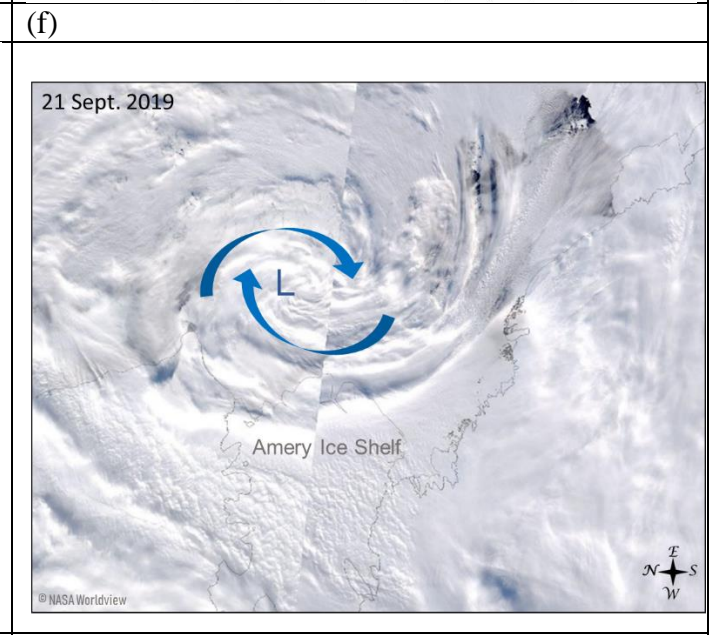
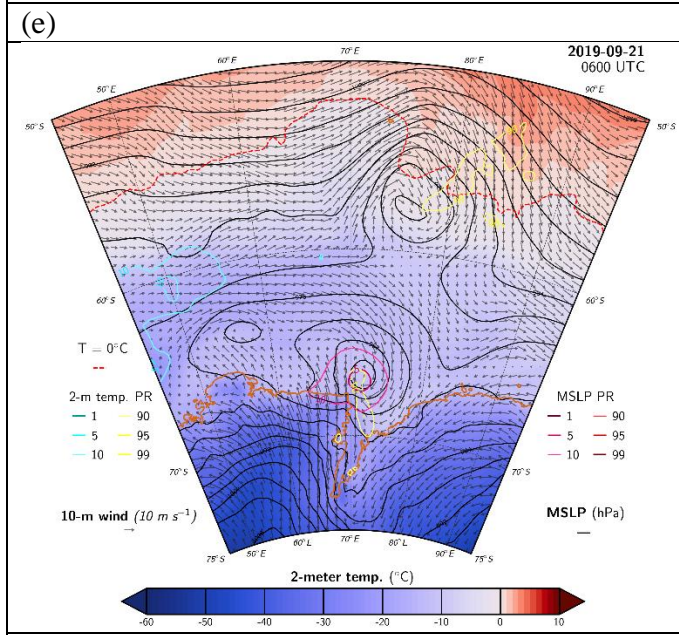
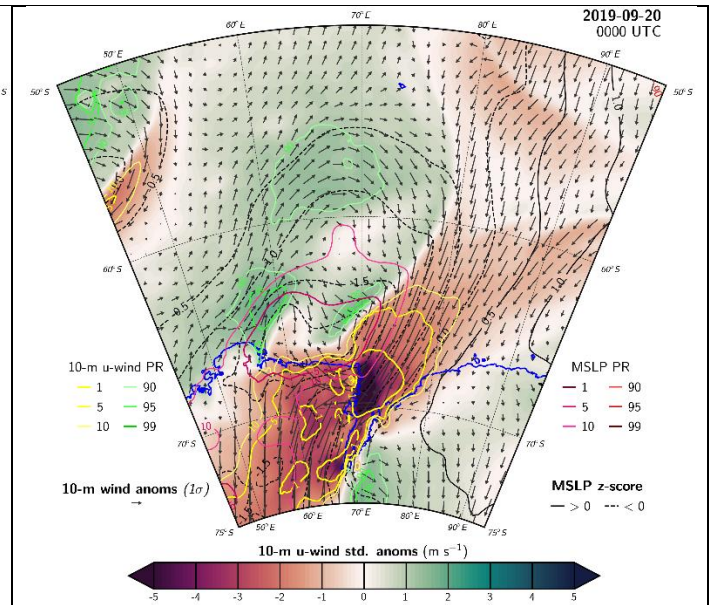
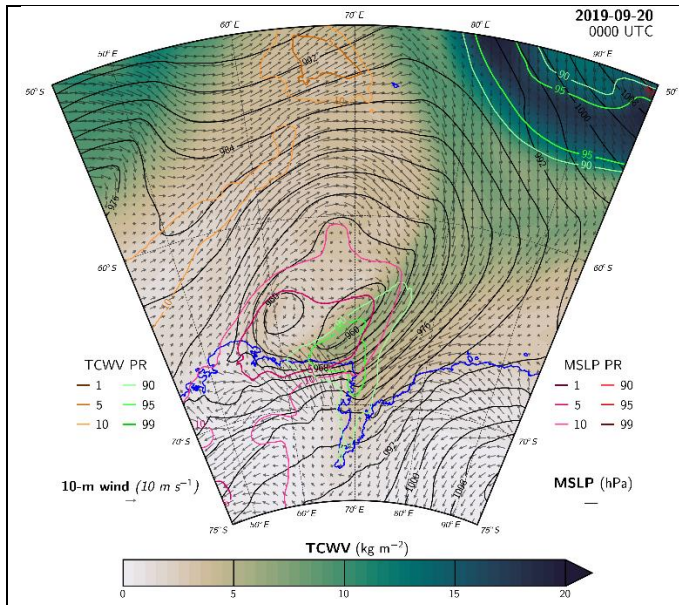
258 decayed on 22 September 2019. Anomalously warm air masses were brought by this cyclone over
 259 the margins of the Amery Ice Shelf exceeding the 90th percentile (Fig. 4e). MODIS satellite
 260 imagery on this day showed a swirling cyclone at the mouth of the Amery Ice Shelf (Fig. 4f).
 261 Sentinel-3A and 3B observations on 22 September 2019 at 0000 UTC (i.e., during the decay of
 262 the cyclones) show elevated sea surface at the ice-shelf front area reaching 6 m significant wave
 263 height (Fig. 4g). Given the easterly direction of the winds associated with the storm during this
 264 episode, the observed elevation of sea surface indicates that storm tide occurred at the ice shelf
 265 front. Furthermore, waves and tides generated by the cyclones during the 18-21 September 2019
 266 period, when easterly wind speeds were stronger, may have been substantially higher.
 267 Unfortunately, sentinel observations are not available during this period over the area of interest
 268 to check this.

269 Surface melt during this event may have occurred briefly due to the anomalous warm and moist
 270 air masses. However, the inspection of daily satellite images of Sentinel-1 backscatter coefficient,
 271 MODIS ice surface temperature and AMSR2 brightness temperature did not show any prolonged
 272 nor significant surface melt at the Amery Ice Shelf during this event.

273 In summary, an extended period of strong cyclonic activity from 18-22 September 2019 resulted
 274 in exceptional period of strong easterly / northeasterly winds over the western side of the Amery
 275 Ice Shelf where the climatology shows a positive zonal component. These exceptional winds
 276 generated significant storm surge onto the ice shelf and helped in preconditioning the breakoff as
 277 it will be discussed in section 2.3.

278 .
 279





(g)

(f)

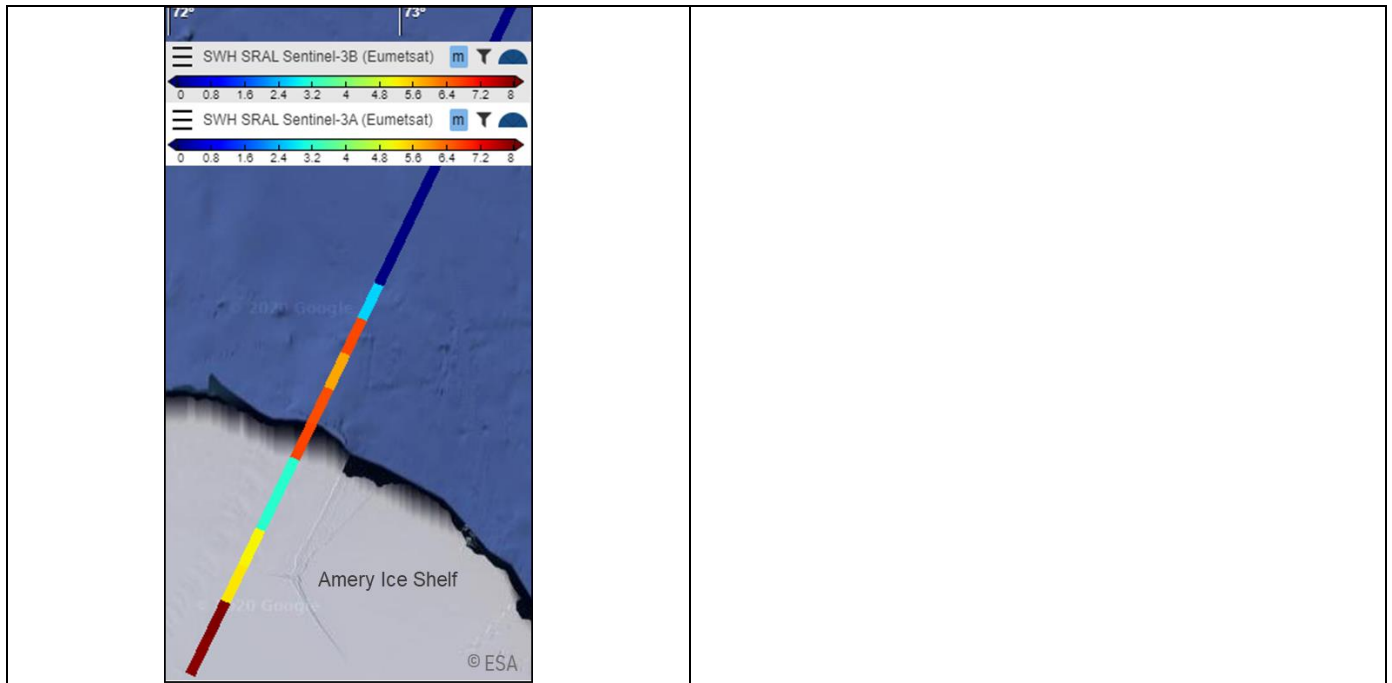


Figure 4: ERA5 reanalysis of: (a) MSLP in colors and winds at 925hPa in vectors on 19 September 2019 at 2200 UTC, (b) 2-m temperature in colors, winds at 925hPa in vectors, MSLP in black contours and 0°C contour in red on 19 September at 2200 UTC, (c) total column water vapor (TCWV) in colors, winds at 925hPa in vectors and MSLP in black contours on 20 September 2019 at 0000 UTC, (d) standardized anomalies relative to the full record (1979-2019) of 10-m u-wind on 20 September 2019 at 0000 UTC. Vectors show 10-m wind anomalies, black contours show positive MSLP anomalies and dashed black contours show negative MSLP anomalies. Colored contour lines show percentile rank extremes (1, 5, 10 and 90, 95, 99 percentile ranks) of the corresponding quantities indicated on the plots, (e) 2-m temperature in colors, 10-m winds in vectors, MSLP in black contours and 0°C contour in red dashed-line on 21 September at 0600 UTC. (f) MODIS visible imagery on 21 September 2019, image credit: NASA worldview. (g) Sentinel-3A and 3B observations of wave height on 22 September 2019 at 0000 UTC, image credit: ESA Ocean Virtual Laboratory.

280

281 **2.2. Twin polar cyclones during 23-24 September 2019 - calving**

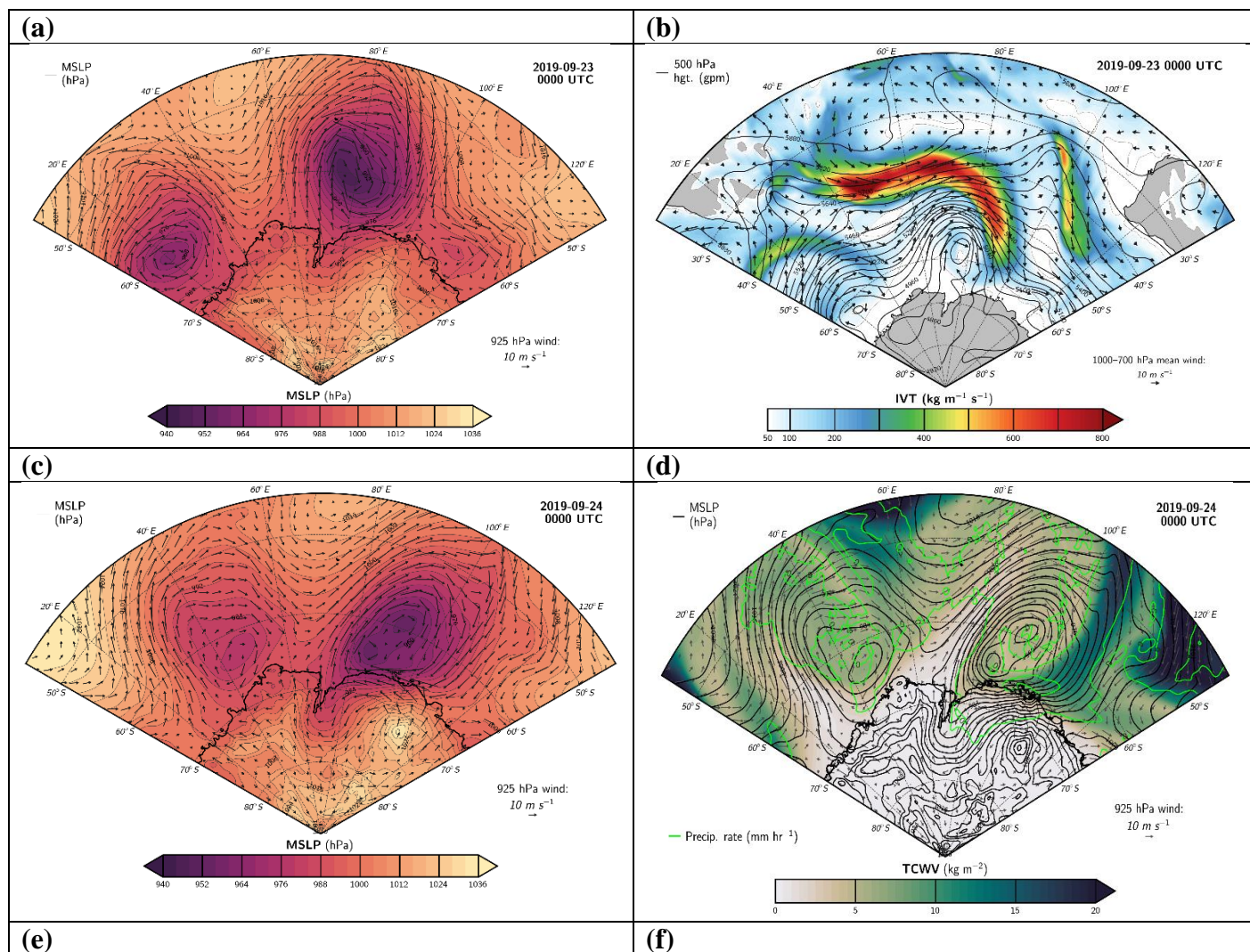
282 Following the extended period of extreme cyclones in Cooperation sea, an explosive cyclone
 283 started to develop on 21 September 2019 centered at 45°E and 60°S. The pressure at its center
 284 deepened from 976hPa on 21 September at 1900 UTC to 952hPa on 22 September 2019 at 19 UTC
 285 (not shown). On 23 September 2019, the large explosive cyclone entered Cooperation Sea from
 286 the west with a deep low of 940 hPa (Fig. 5a). It was accompanied by an intense atmospheric river
 287 exhibiting core IVT greater than $800 \text{ kg m}^{-1} \text{ s}^{-1}$ and stretching from mid-latitudes towards
 288 Antarctica (Fig. 5b). The explosive cyclone was stationary over Cooperation Sea during the whole
 289 day on 23 September 2019, being trapped between two far-south-reaching blocking highs one to
 290 the west of it and the second to its east (Fig. 5a and 5c). The cyclone intensified, increased in size
 291 and evolved into twin cyclones on 24 September 2019 at 0000 UTC associated with 952hPa low
 292 pressure at their respective centers (Fig. 5c and 5d). The mutual interaction between the two
 293 cyclones appeared as co-rotation and an eastward translation of the binary pair by the ambient

294 flow. The interplay between the cyclones lasted for one day after which the twins merged and
295 decayed on 25 September 2019.

296 To the south of the twin cyclones, a cold pressure high (1036 hPa) developed over the ice sheet as
297 a result of the accumulation of cold air due the blocking ridge to the northeast (Fig. 5c). The high-
298 pressure advected very cold air (2-m temperature below -40°C) into the twin-cyclone system (Fig.
299 5e and 5 f) which may have fostered baroclinicity and frontogenesis, hence sustaining the twin
300 cyclones for a longer period of time.

301 The atmospheric river continued to advect large amounts of moisture and precipitation occurred
302 over a large area (Fig. 5d). Sustained advection of exceptionally warm air masses was observed
303 during this event as well (Fig. 5e and 5f). Air masses characterized by 0°C 2-m temperatures were
304 seen to penetrate further south reaching 66°S over the region to the east of the twin cyclones during
305 the whole day on 24 September 2019 (Fig. 5e and 5f).

306



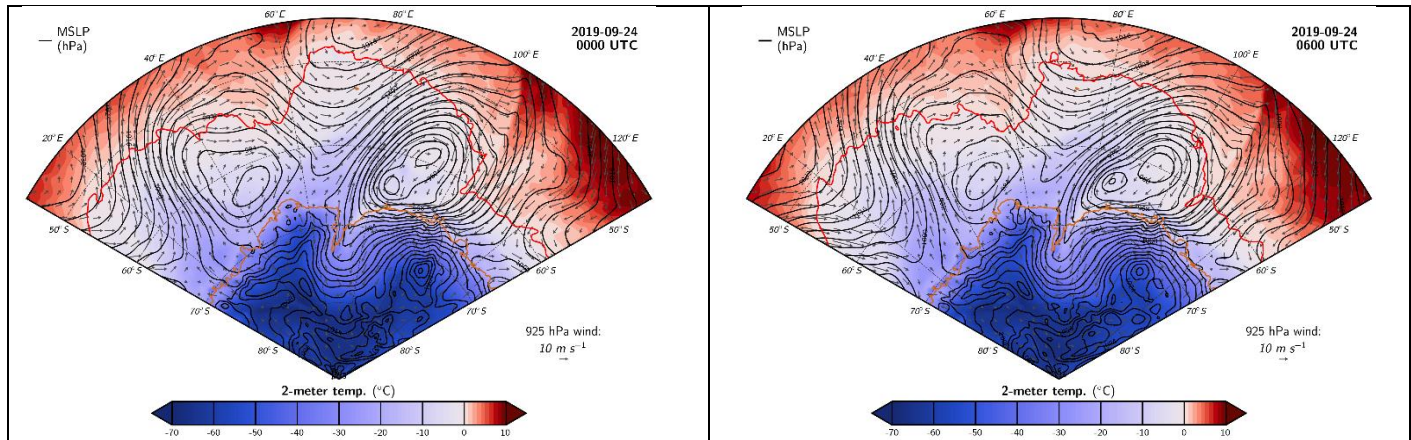
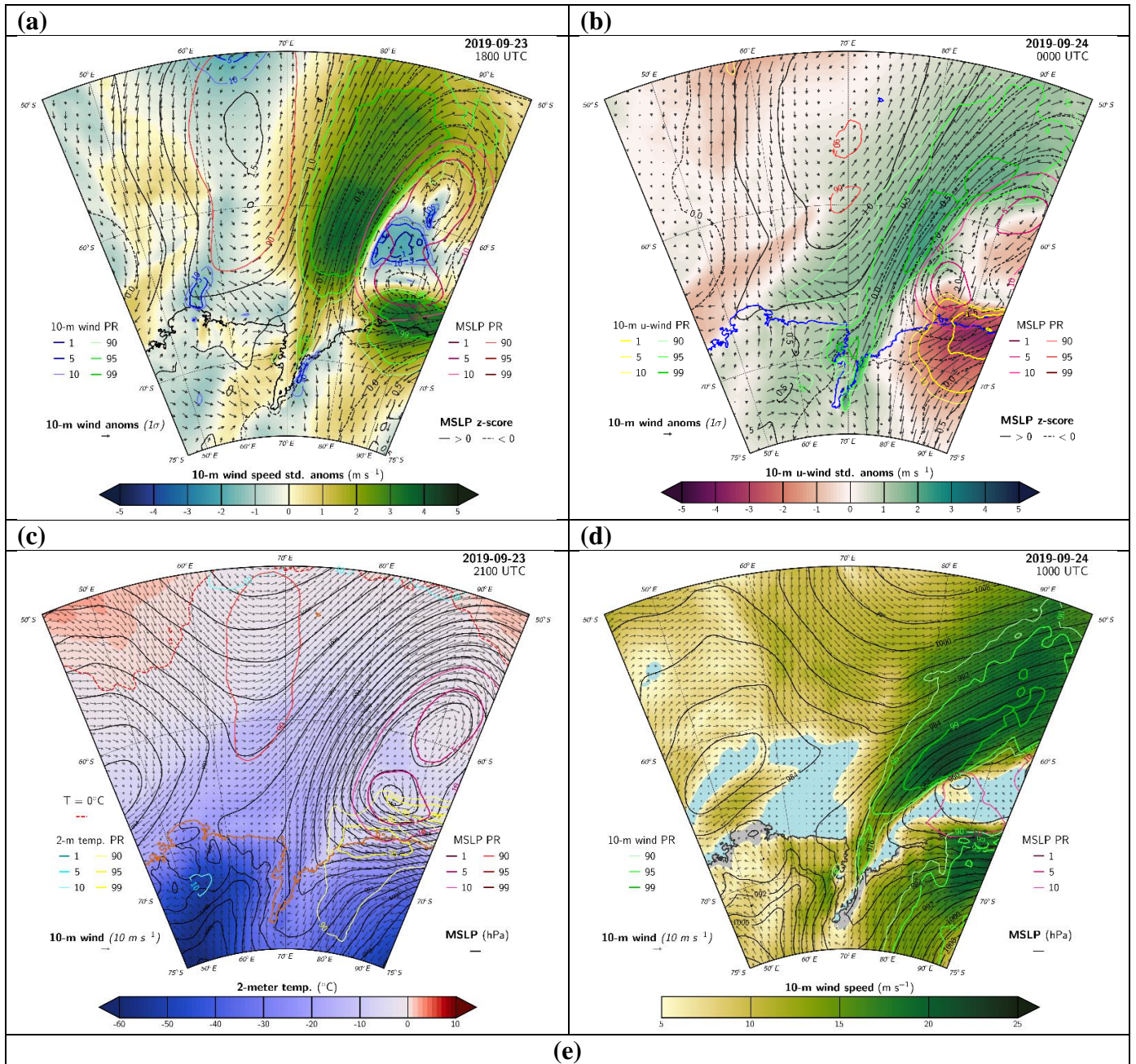


Figure 5: (a) MSLP in colors and winds at 925hPa in vectors on 23 September 2019 at 0000 UTC, (b) integrated water vapor transport (IVT) in colors, geopotential heights at 500 hPa in black contours and 1000-700 hPa mean winds in black vectors on 23 September 2019 at 0000 UTC, (c) MSLP in colors and winds at 925hPa in vectors on 24 September 2019 at 0000 UTC, (d) total column water vapor (TCWV) in colors, winds at 925hPa in vectors, precipitation rate in green contours and MSLP in black contours on 24 September 2019 at 0000 UTC, (e) 2-m temperature in colors, winds at 925hPa in vectors, MSLP in black contours and 0°C contour in red on 24 September at 0000 UTC, (f) same as (e) but at 0600 UTC.

307

308 During 23-24 September, the deep twin polar cyclones were stationary to the east of the Amery
 309 Ice Shelf (Fig. 5) associated with MSLP anomalies at their centers below the 5th percentile (Fig.
 310 6a and 6c). They induced extreme westerlies (10-m wind speed in the order of 17 m s^{-1}) across the
 311 ice shelf with positive 10-m wind anomalies exceeding 2 standard deviations from the
 312 climatological mean (Fig. 6a). The direction of the winds was also exceptional with above 99th
 313 percentile u-wind over the western ice shelf margin from 23 September 2019 at 1800 UTC (Fig.
 314 6b) through 24 September 2019 at 1200 UTC and below the 5th percentile u-wind values over the
 315 lower eastern ice shelf area (Fig. 6a and 6b). Weaker but still significant (95 percentile) westerly
 316 wind anomalies lingered during the remainder of the day on 24 September 2019 and through
 317 midday on 25 September 2019 with wind speed at 10-m reaching 15 m s^{-1} at the front of the ice
 318 shelf (Fig. 6d). Sustained positive 2-m temperature anomalies were observed throughout the twin
 319 cyclone event over the eastern side of Prydz Bay. Warm air advection by the twin cyclones brought
 320 95 percentile rank temperatures over the eastern side of the Amery Ice Shelf and Prydz Bay on 23
 321 and 24 September 2019 and 90 percentile rank temperatures inland over Princess Elizabeth Land
 322 (Fig. 6c). These episodes of poleward advection of warm air masses may explain the observed
 323 positive-trend in surface temperatures during winter/spring seasons at Prydz Bay reported by Heil
 324 (2006) using measurements from ground stations.

325 The distribution of hourly 10-m wind speed for all months 1979-2019 over the Amery Ice Shelf
 326 front is shown in the histogram in Fig. 6f. The winds during the 18-22 September 2019 period
 327 were exceptionally unusual compared to the record. The winds during the 23-25 September 2019
 328 period were strong but not unusually extreme. This suggests that the first extreme cyclones' event
 329 had an important role in preconditioning the ice shelf front for breakoff, while the offshore winds
 330 during the second event triggered the calving along the T1 rift.



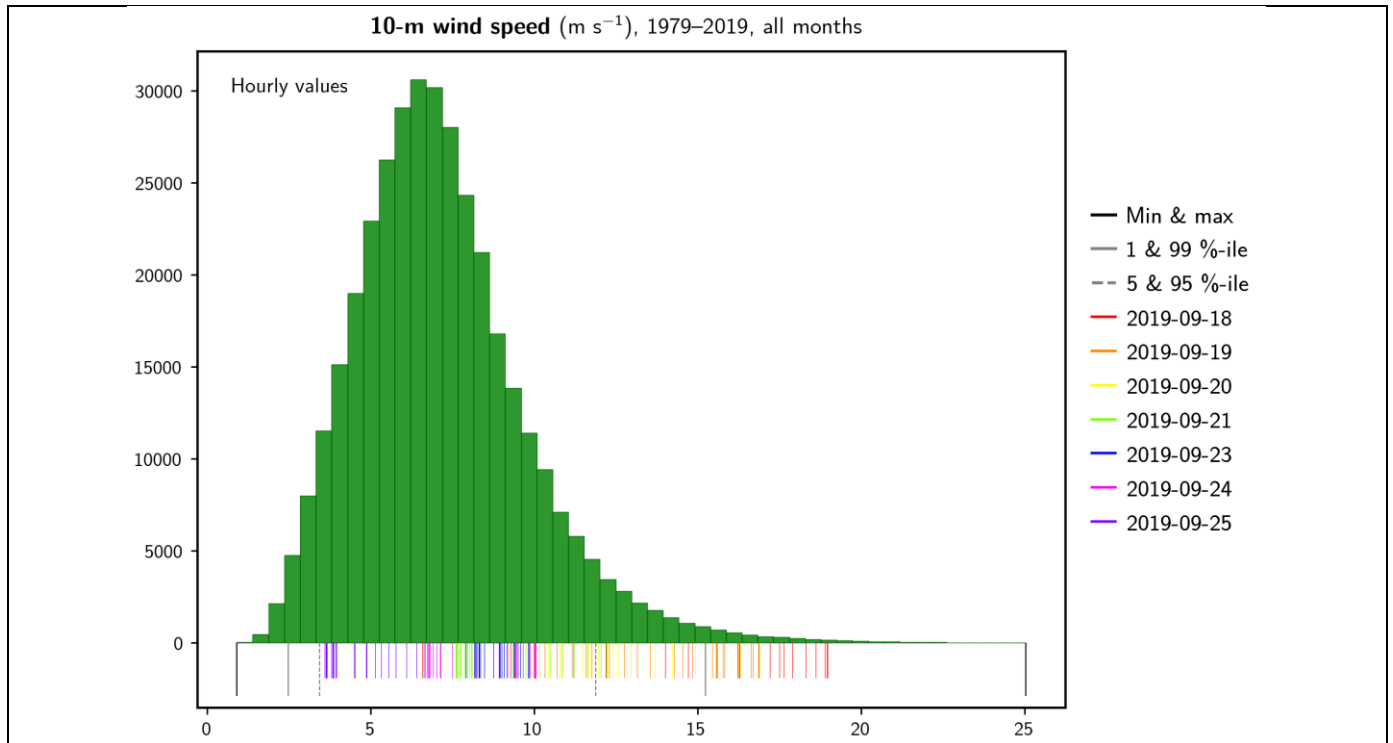


Figure 6: (a) Standardized anomalies relative to the full September record (1979-2019) of 10-m wind speed (colors) at 23 September 2019 1800 UTC. (b) Same as (a) but with u-component of 10-m wind as filled contours at 24 September 2019 0000 UTC. Vectors show 10-m wind anomalies, black contours show positive MSLP anomalies and dashed black contours show negative MSLP anomalies. Colored contour lines show percentile rank extremes (1, 5, 10 and 90, 95, 99 percentile ranks) of the corresponding quantities indicated on the plots. (c) 2-m temperature in colors, winds at 925hPa in vectors, MSLP in black contours and 0°C contour in red dashed-line on 23 September at 2100 UTC. (d) 10-m wind speed in colors, 10-m wind direction in black vectors and MSLP in black contours on 24 September 2019 at 1000 UTC. (e) Histogram showing the distribution of hourly 10-m wind speed for all months during 1979-2019, spatially averaged over 70-65°S and 70-75°E. The colored vertical lines correspond to hourly values during the 18-25 September 2019 period. Each given day in September 2019 has 24 hourly values plotted in the same color.

332

333 2.3 The calving

334 The anomalous atmospheric conditions during the extended period of strong cyclonic activity
 335 occurring over the ice cover in Cooperation and Davis Seas (i.e., south to the sea ice edge)
 336 impacted the state of the ocean in front of and around the Amery Ice Shelf. The storm surge caused
 337 by the first twin cyclones (i.e., Fig. 4g) was followed by an ocean ward slope induced by the second
 338 episode of cyclones. Fig. 7a shows a clear increase in maximum ocean slope close to the Amery
 339 Ice Shelf in the period prior to the calving (0.05 degrees slope anomaly). The wind pattern of 23-
 340 24 September induced a significant slope on the ocean surface at/near the ice front. This ocean
 341 ward slope tugs on the ice front, placing extensional stress on the pre-existing rift. The SAR
 342 satellite image on 23 September 2019 together with the ice-displacement velocity (rate and
 343 direction in vectors) relative to 11 September 2019 are shown in Fig. 7b. The displacement vectors

344 indicate that the iceberg-to-be was rotating in the period 11-23 September 2019 prior to the calving.
345 Wind-induced ocean slope caused a leftward (relative to the rift T1) splitting-movement of the
346 future iceberg prior to break-off on 25 September 2019. This caused rapid opening of the crack
347 and subsequent movement of the iceberg away from the ice shelf (Fig. 8a).

348 The extreme nature and long duration of the cyclones during both cyclones' episodes resulted in
349 sustained tides and ocean ward slope of the sea surface, consecutively. Between the previous storm
350 event and the 23-24 September storm, there was a rapid change from a shoreward surge to ocean
351 slope away from the ice front. This put strain on the pre-existing rift at the front of the Amery Ice
352 Shelf leading to rift growth and calving.

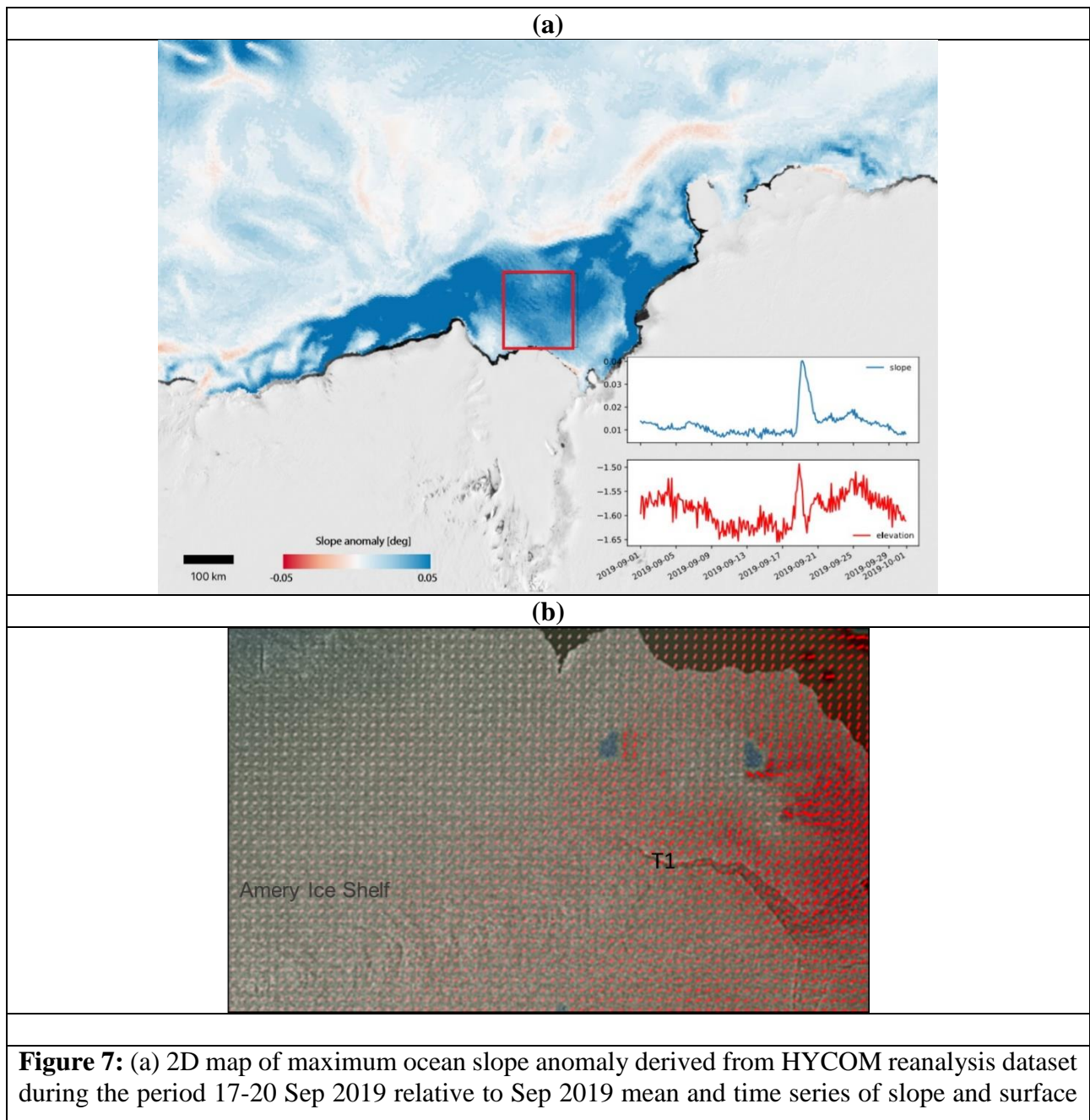


Figure 7: (a) 2D map of maximum ocean slope anomaly derived from HYCOM reanalysis dataset during the period 17-20 Sep 2019 relative to Sep 2019 mean and time series of slope and surface

elevation over the red bounding box showed on the map. (b) SAR image of the Amery Ice Shelf on 23 September 2019. The red vectors correspond to the ice displacement on 23 September 2019 (both velocity and direction) relative to 11 September 2019.

353

354 **2.4 Sea ice conditions**

355 The action of strong winds on sea ice removal from the area at the mouth of the Amery Ice Shelf
356 was visible in MODIS imagery as well as in the satellite observations of sea ice concentration and
357 drift (Fig. 8). During the period of the twin polar cyclones on 23- 24 September 2019, the sea ice
358 was pushed about 65 km away from the ice shelf front in just a 2-day period of time (Fig. 8a). The
359 ice-free region in front of the ice shelf presented an asymmetric shape where the sea ice in front of
360 the western side of the ice shelf was pushed further away compared to the sea ice in front of the
361 eastern side (Fig. 8a). This may have made the western side more vulnerable to the winds and
362 associated tide/ocean slope induced by the consecutive explosive cyclones.

363 Moreover, sea ice concentration in Cooperation Sea and at the Amery Ice Shelf front area was
364 reduced to below 60%, reaching 40% in some places (Fig. 8b and 8c). By the end of the intense
365 cyclonic activity period, areas of open water formed especially at the locations of the strongest
366 surface winds i.e., to the west of the twin cyclones centers (Fig. 8b and 8c). Significant reduction
367 in sea ice concentration was also observed along the sea ice edge associated with wind-driven
368 currents and waves (Fig. 8b).

369 Significant sea ice drift was observed at the mouth of the Amery Ice Shelf associated with the
370 exceptional westerlies generated by the twin cyclones on 23-24 September 2019 (Fig. 8c). The sea
371 ice drift velocity during this period reached 50 km on average per day and the sea ice drifted away
372 from the Amery Ice Shelf towards the east and northeast (Fig. 8c).

373 Sea ice loss in the vicinity of weakened or flooded shelves is considered as a contributor factor to
374 rapid ice shelf calving (e.g., Massom et al., 2018). The removal of the protective buffer represented
375 by sea ice for ice shelves (e.g., Massom et al., 2018) may have increased the effect of the ocean
376 ward slope on the outer ice shelf western margin and helped in the gravitationally-induced calving.

377 Explosive cyclones crossing the sea ice zone around Antarctica can generate waves of up to 8
378 meters in height that are capable of propagating more than 100 km into the sea ice cover (Vichi et
379 al., 2019). The consecutive deep cyclones under scrutiny impacted immediately the Amery Ice
380 Shelf front since they were found very close to the coast. During the first period of explosive twin
381 cyclones, the cyclones were sitting to the west of the Amery Ice Shelf which directed anomalous
382 warm and moist easterlies towards it. This situation caused shoreward storm surge and tide
383 immediately at the shelf front (Fig. 4g). This was then followed by additional extreme atmospheric
384 forcing brought by the second event of explosive twin cyclones, producing strong offshore winds,
385 sea ice removal and ocean ward sea surface slope. This combination of factors weakened the ice
386 shelf front and made it more vulnerable, resulting in amplification of the fractures along the pre-
387 existing rifts and leading ultimately to its calving.

388 Previous studies (Holdsworth and Glynn, 1978; Squire et al., 1994) have shown that calving ice
389 shelves can be triggered by wind-induced waves which impose flexural strains on the ice shelves,

390 with the potential to induce crevasse and rift propagation and calving (Robinson and Haskell, 1992;
 391 Bromirski et al., 2010). This effect can be even maximized by the loss of the protective sea ice
 392 pack at the front of the ice shelves (Massom et al., 2018). Here we have shown that the series of
 393 intense cyclones provided ideal conditions for both sea ice reduction, wind-tides and ocean slope
 394 and ultimately triggered the calving on 25 September 2019.

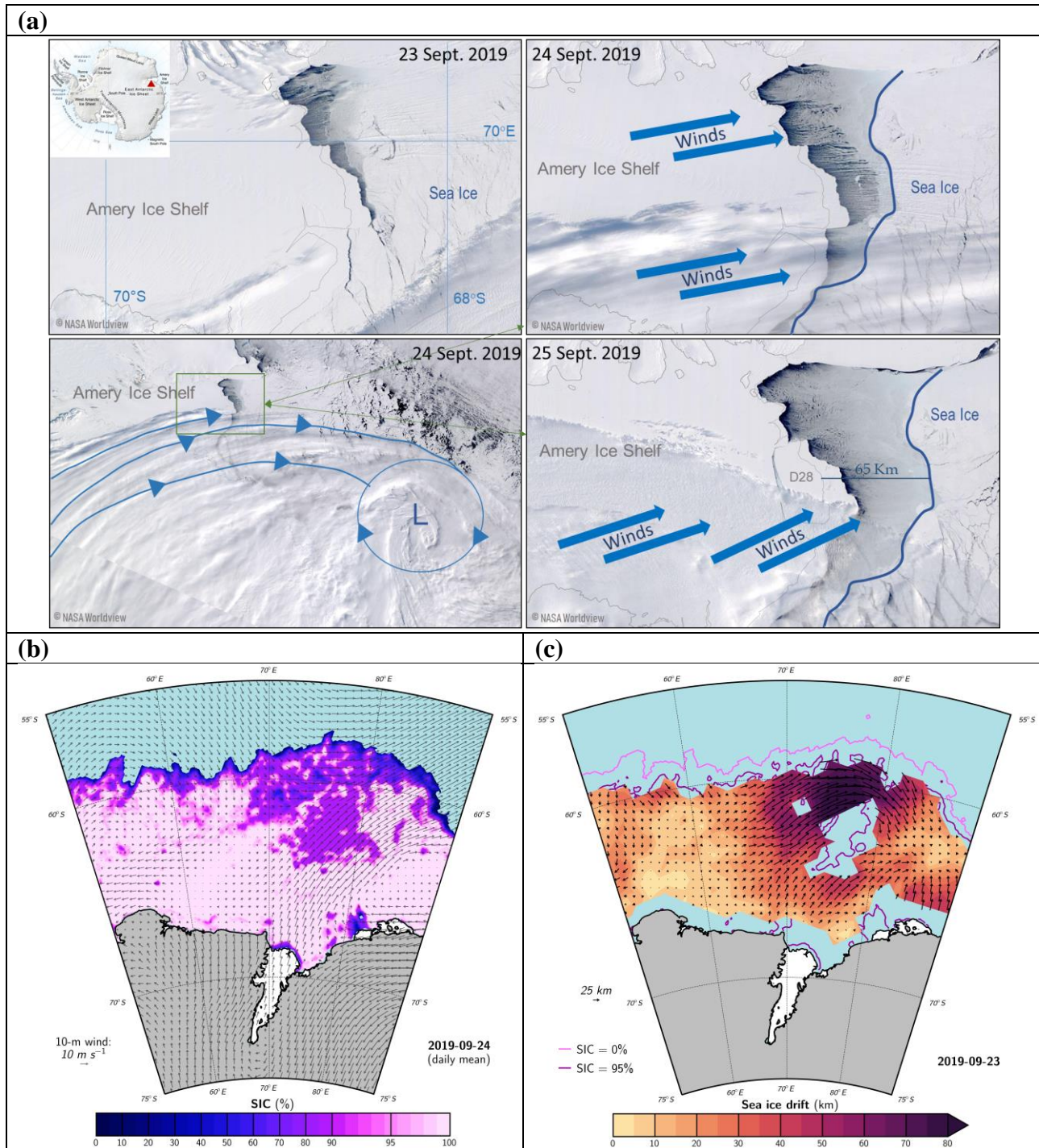


Figure 8: (a) MODIS satellite visible imagery of the Amery Ice Shelf showing the ice shelf before the calving on 23 September 2019, during the calving on 24-25 September 2019. Image credit:

NASA Worldview. (b) Satellite-derived sea ice concentrations and ERA5-derived daily mean 10-m winds in vectors over 55-75S and 50-90E on 24 September 2019 at 0000 UTC. (c) Satellite-derived daily sea-ice drift velocity in colors and direction in vectors on 23 September 2019. The solid pink contour is the 0% sea ice concentration contour and the solid purple contour is the 95% sea ice concentration contour.

395

396 **3. Discussion and conclusions**

397 In this study, the role of atmospheric extremes in the recent calving of the Amery Ice Shelf in
398 September 2019 is addressed by investigating the atmospheric conditions in combination with the
399 ice and ocean state. During the month of September 2019, the circulation around Antarctica was
400 characterized by anomalously-pronounced 3 ridges and 3 troughs with the Indian sector of the
401 Southern Ocean being under the influence of troughing and surrounded by two blocking ridges;
402 one over the southern Atlantic to the west and one over Davis Sea and southern Australia to the
403 east.

404 During the second half of September 2019, a series of explosive polar cyclones, evolving into
405 stationary twin polar cyclones, impacted the region of the Amery Ice Shelf. The first explosive
406 cyclone occurred on 18 September 2019 and evolved into two stationary twin polar cyclones on
407 19-22 September 2019 sitting to the west of the ice shelf. The second explosive cyclone formed
408 on 23 September 2019 and evolved into two stationary twin polar cyclones on 24-25 September
409 2019, sitting, this time, to the east of the Amery Ice Shelf. Both explosive-cyclone episodes were
410 accompanied by intense atmospheric rivers bringing anomalous warm and moist air masses
411 poleward. The stationary aspect of the deep cyclones had a large impact on the ice conditions as it
412 subjected the ice to sustained stress and strain. The main difference between the two episodes is
413 the location at which the twin cyclones were stationary, relative to the Amery Ice Shelf, which
414 determined the characteristics of the air masses and the wind direction that affected the ice shelf.
415 This position of the cyclones relative to the Amery Ice Shelf was, in turn, determined in each
416 episode, by the location of the blocking ridges in the general circulation.

417 During the first episode, anomalous warm, moist and easterly winds impacted the ice shelf and
418 surrounding sea ice, whereas during the second episode, the ice shelf and surrounding sea ice were
419 under the influence of anomalous westerlies. The first episode resulted in a shoreward storm surge
420 at the front of the ice shelf. During the second episode, anomalously strong offshore winds resulted
421 in an ocean ward slope and an ice-free area in front of the western side of the ice shelf. The
422 sustained strong winds and associated sea surface slope toward the open ocean maintained a strain
423 on the shelf-front and amplified the fracture along the pre-existing rift leading to the calving.

424 The detached iceberg after calving followed a northeasterly motion being dragged by the
425 prevailing winds and associated ocean currents. This drifting direction was similar to the one
426 followed by the sea ice one day before and gave an indication of the impact of the wind direction
427 on this process. Given the east-exposed orientation of the crack at the ice shelf-front, the direction
428 of the sustained strong westerly winds was deterministic for the calving.

429 In summary, atmospheric forcings by the explosive twin polar cyclones induced a gravitationally-
430 driven calving at the Amery Ice Shelf in September 2019 via storm tide and subsequent ocean
431 ward sea-surface slope.

432 The analysis of this unique event could help better understand the underlying factors triggering the
433 calving of ice shelves and hence improve the modelling capabilities of ice shelf future evolution
434 their possible contribution to sea level rise. Our analysis highlights the need for ice sheet models,
435 used to project sea level rise, to account for atmospheric forcing at high resolution, in addition to
436 sea ice and ocean waves, if they were to simulate accurately the changes occurring in the ice sheet
437 and glaciers and their contribution to sea level rise.

438 In fact, important changes in the atmospheric circulation are being observed in the Southern
439 Hemisphere. For instance, between 1979 and 2010 the subtropical jet streams moved poleward by
440 6.5 ± 0.2 degrees in the Southern Hemisphere (Hudson, 2012) and the westerlies strengthened and
441 shifted poleward (Fogt and Marshal, 2020). The observed poleward movement over the past few
442 decades represents a significant change in the position of the sub-tropical jet stream, which should
443 lead to significant latitudinal shifts in the global weather patterns, the hydrological cycle and their
444 impact on Antarctic ice shelves.

445 The variability of the polar jet front in the Southern Hemisphere and whether similar behavior as
446 the polar jet in the Northern Hemisphere is underway around Antarctica needs to be investigated
447 in future work. Several studies have shown evidence for a wavier jet stream in response to rapid
448 Arctic warming and reported a weakening of the polar jet as a result of a reduced temperature
449 gradient between high and mid-latitudes due to the increased temperatures in the Arctic (e.g.,
450 Francis and Vavrus, 2015; Coumou et al., 2015; Mann et al., 2017). Such change in the polar jet,
451 which acts as an isolation boundary between high and mid latitudes, would lead to more
452 interactions, and spark feedback mechanisms between the Antarctic system and mid-latitudes as it
453 happened to be the case in the Arctic (Francis et al., 2018; 2019b).

454 The poleward shift of the cyclones together with the decrease in sea ice extent in recent years
455 makes it more urgent to assess the impact of cyclones on Antarctic-wide maritime-terminating ice
456 shelves as higher numbers of large cyclones could be expected to reach further south and therefore
457 affects ice shelves dynamics. If extreme polar cyclones are to form or reach more frequently ice
458 shelves due to climate change, their destructive effect may have important consequences and needs
459 to be accounted for in models used for sea level and Antarctic Ice Sheet mass balance projections.

460 **4. Data and methods**

461 The atmospheric analysis is based on data from the ERA5 reanalysis (Hersbach et al., 2020).
462 During the period 16-25 September 2019, hourly maps of mean sea level pressure (MSLP), winds,
463 2m temperature and total column water vapor (TCWV) are analyzed. Furthermore, in order to
464 investigate the anomalous character of the atmospheric conditions, we calculated, for the same
465 period and quantities listed above, hourly standardized anomalies and percentile ranks relative to
466 all hourly ERA5 September values during the full record (1979-2019) over the area 45-95°E, 50-
467 75°S. In addition, a histogram analysis has been performed over a smaller domain limited to the
468 ice-shelf front area and adjacent mouth of Prydz Bay (i.e., 70-65°S and 70-75°E). The histograms

469 represent the distribution of hourly values spatially averaged over this domain, for all months
470 during 1979-2019.

471 Daily sea ice extent and concentration data are derived from the AMSR-E / AMSR2 unified record
472 (Meier et al., 2018) at 12.5 km spatial resolution (https://nsidc.org/data/AU_SII2/versions/1). To
473 check the motion in the sea ice field in the Amery Basin, we used the low-resolution sea ice drift
474 product of the EUMETSAT Ocean and Sea Ice Satellite Application Facility (OSI SAF, [www.osi-
475 saf.org](http://www.osi-saf.org)). This is a 48-hour average gridded ice drift dataset processed on a daily basis and made
476 available on a 62.5 km Polar Stereographic Grid (e.g., Kwok et al. 2017). Ice motion vectors are
477 estimated by an advanced cross-correlation method on pairs of satellite images (Lavergne et al.,
478 2010). It uses the multi-sensor spatial covering product that combines SSMIS (91 GHz H and V
479 polarization) on board DMSP platform F17, ASCAT (C-band backscatter) on board EUMETSAT
480 platform Metop-A, and AMSR-2 on board JAXA platform GCOM-W. Due to atmospheric noise
481 and surface melting these data are only available for the Southern Hemisphere winter (1st April to
482 31st October).

483 Visible imagery of the Amery Ice Shelf and surrounding area are taken from MODIS/VIIRS land
484 products (ORNL DAAC, 2018) using the NASA Worldview application
485 (<https://worldview.earthdata.nasa.gov>).

486 Sentinel-1 data has been used to determine potential surface melt (e.g., Datta et. al, 2019) and to
487 track ice velocity over the Amery ice shelf prior to the D28 iceberg calving by using feature
488 tracking in ESA's SNAP Sentinel-1 toolbox. Sentinel-3A and 3B data were used via the ESA
489 Ocean Virtual Laboratory application to determine the wave height at the front of the Amery Ice
490 Shelf.

491 The ocean slope and elevation are taken from the Hybrid Coordinate Ocean Model (HYCOM,
492 <https://www.hycom.org/>). HYCOM (Cummings and Smedstad, 2013) is a data-assimilative hybrid
493 isopycnal-sigma-pressure (generalized) coordinate ocean model of which we downloaded
494 elevation from the Google Earth Engine at 0.08-degree latitude/longitude grid. Based on this
495 elevation dataset, the surface slope was derived as the local gradient using the 4-connected
496 neighbors of each pixel.

497 **Acknowledgments**

498 We acknowledge the use of imagery from the NASA Worldview application
499 (<https://worldview.earthdata.nasa.gov>), part of the NASA Earth Observing System Data and
500 Information System (EOSDIS). This work was supported by Masdar Abu Dhabi Future Energy
501 Company, United Arab Emirates, Grant 8434000221. The contribution of Petra Heil was supported
502 by the Australian Government's Australian Antarctic Partnership Program, and contributes to AAS
503 Project 4506.

504 **Code and Data availability:** All data needed to evaluate the conclusions in the paper are present
505 in the paper. Correspondence and requests for materials should be addressed to DF.

506 **Author contributions** D.F. conceived the study and wrote the initial manuscript. K.M. analyzed
507 the satellite and reanalysis data. S.L analyzed satellite data. M.T. and P.H. provided input on result
508 analysis. All authors interpreted results and provided input to the final manuscript.

509 **Competing Interests** The authors declare that they have no competing interests.

510

511 **References**

- 512 1. Allen, J.T., Pezza, A. B., and Black, M. T. (2010) Explosive cyclogenesis: a global climatology
513 comparing multiple reanalyses. *Journal of Climate*, v.23, 6468–6484.
- 514 2. Aitken, A., Roberts, J., Ommen, T. et al. Repeated large-scale retreat and advance of Totten
515 Glacier indicated by inland bed erosion. *Nature* 533, 385–389 (2016).
516 <https://doi.org/10.1038/nature17447>.
- 517 3. Barnes, E. A., and L. Polvani (2013), Response of the midlatitude jets, and of their variability,
518 to increased greenhouse gases in the CMIP5 Models, *J. Clim.*, 26, 7117– 7135.
- 519 4. Bassis, J., Fricker, H., Coleman, R., & Minster, J. (2008). An investigation into the forces that
520 drive ice-shelf rift propagation on the Amery Ice Shelf, East Antarctica. *Journal of Glaciology*,
521 54(184), 17-27. doi:10.3189/002214308784409116.
- 522 5. Bassis, J. N. and Ma, Y.: Evolution of basal crevasses links ice shelf stability to ocean forcing,
523 *Earth Planet. Sci. Lett.*, 409, 203–211, <https://doi.org/10.1016/j.epsl.2014.11.003>, 2015.
- 524 6. Bengtsson, L., K. I. Hodges, and N. Keenlyside (2009), Will extratropical storms intensify in
525 a warmer climate? *J. Clim.*, 22(9), 2276– 2301.
- 526 7. Benn D. I. and J. A. Åström (2018) Calving glaciers and ice shelves, *Advances in Physics: X*,
527 3:1, DOI: 10.1080/23746149.2018.1513819.
- 528 8. Bromirski, P. D., Sergienko, O. V. & MacAyeal, D. R. Transoceanic infragravity waves
529 impacting Antarctic ice shelves. *Geophys. Res. Lett.* 37, L02502 (2010).
- 530 9. Brunt, K., Okal, E., & MacAyeal, D. (2011). Antarctic ice-shelf calving triggered by the
531 Honshu (Japan) earthquake and tsunami, March 2011. *Journal of Glaciology*, 57(205), 785-
532 788. doi:10.3189/002214311798043681.
- 533 10. Chang, E. K. M., Y. Guo, and X. Xia (2012), CMIP5 multimodel ensemble projection of storm
534 track change under global warming, *J. Geophys. Res.*, 117, D23118,
535 doi:10.1029/2012JD018578.
- 536 11. Chang, E. K. M., 2017: Projected Significant Increase in the Number of Extreme Extratropical
537 Cyclones in the Southern Hemisphere. *J. Climate*, 30, 4915–4935,
538 <https://doi.org/10.1175/JCLI-D-16-0553.1>.
- 539 12. Cook, A. J. and Vaughan, D. G.: Overview of areal changes of the ice shelves on the Antarctic
540 Peninsula over the past 50 years, *The Cryosphere*, 4, 77–98, [https://doi.org/10.5194/tc-4-77-](https://doi.org/10.5194/tc-4-77-2010)
541 2010, 2010.
- 542 13. Coumou D., J. Lehmann, J. Beckmann, (2015), The weakening summer circulation in the
543 Northern Hemisphere mid-latitudes, *Science*, Vol. 348, Issue 6232, pp. 324-327. DOI:
544 10.1126/science.1261768.
- 545 14. Cummings, J.A. and O.M. Smedstad, 2013: Variational data analysis for the global ocean. In:
546 S.K. Park and L. Xu (Eds.), *Data Assimilation for Atmospheric, Oceanic and Hydrologic*

- 547 Applications Vol. II., DOI 10.1007/978-3-642-35088-7_13, Springer-Verlag Berlin
548 Heidelberg.
- 549 15. Datta, R. T. Tedesco, M., Fettweis, X., Agosta, C., Lhermitte, S., Lenaerts, J.T.M., Wever, N.
550 (2019) The Effect of Foehn-Induced Surface Melt on Firn Evolution Over the Northeast
551 Antarctic Peninsula. *Geophys. Res. Lett.* 46, 3822–383, doi: 10.1029/2018GL080845.
- 552 16. Davies, H. C., 1997: Emergence of the mainstream cyclogenesis theories. *Meteor. Z.*,6, 261–
553 274.
- 554 17. DeConto, R., Pollard, D. Contribution of Antarctica to past and future sea-level rise. *Nature*
555 531, 591–597 (2016), <https://doi.org/10.1038/nature17145>.
- 556 18. Dolatshah, A., Nelli, F., Alberello, A., Bruneau, L., Bennetts, L. G., Meylan, M. H., Monty, J.
557 P., and Toffoli, A. "Wave Attenuation due to Ice Cover: An Experimental Model in a Wave-
558 Ice Flume." Proceedings of the ASME 2017 36th International Conference on Ocean, Offshore
559 and Arctic Engineering. Volume 8: Polar and Arctic Sciences and Technology; Petroleum
560 Technology. Trondheim, Norway. June 25–30, 2017. V008T07A016. ASME.
561 <https://doi.org/10.1115/OMAE2017-61548>.
- 562 19. Darji S., S.R. Oza, R. D. Shah, B. P. Rathore and I. M. Bahuguna, 2018: Rift assessment and
563 potential calving zone of Amery Ice Shelf, East Antarctica. *Current Science*, 115, 1799-1804,
564 doi: 10.18520/cs/v115/i9/1799-1804.
- 565 20. Eayrs, C., Holland, D. M., Francis, D., Wagner, T. J. W., Kumar, R., & Li, X. (2019).
566 Understanding the seasonal cycle of Antarctic sea ice extent in the context of longer-term
567 variability. *Reviews of Geophysics*. 57, 1037– 1064, <https://doi.org/10.1029/2018RG000631>.
- 568 21. Ferreira, R. N., W. N.Schubert, and J. J.Hack, 1996: Dynamical aspects of twin tropical
569 cyclones associated with the Madden–Julian oscillation.*J. Atmos. Sci.*, 53, 929–945.
- 570 22. Francis J. A. and S. J. Vavrus, 2015, Evidence for a wavier jet stream in response to rapid
571 Arctic warming, *Environ. Res. Lett.* 10 014005.
- 572 23. Francis D., C. Eayrs, J-P. Chaboureaud, T. Mote, D. Holland (2018), "Polar jet associated
573 circulation triggered a Saharan cyclone and derived the poleward transport of the African dust
574 generated by the cyclone" *Journal of Geophysical Research: Atmospheres*.
575 DOI:10.1029/2018JD029095.
- 576 24. Francis D., C. Eayrs, J. Cuesta, D. Holland (2019a), Polar cyclones at the origin of the
577 reoccurrence of the Maud Rise Polynya in austral winter 2017, *Journal of Geophysical*
578 *Research: Atmospheres*,124. <https://doi.org/10.1029/2019JD030618>, 2019.
- 579 25. Francis D., C. Eayrs, J-P. Chaboureaud, T. Mote, D. Holland (2019b), A meandering polar jet
580 caused the development of a Saharan cyclone and the transport of dust toward Greenland, *Adv.*
581 *Sci. Res.*, 1, 1–8, <https://doi.org/10.5194/asr-16-49-2019>, 2019.
- 582 26. Francis D., K.S. Mattingly, N. Alshamsi, M. Temimi, R. Massom, P. Heil, 2020, On the crucial
583 role of atmospheric rivers in the two major Weddell Polynya events in 1973 and 2017 in
584 Antarctica. *Sci. Adv.* 6, eabc2695 (2020).
585 <https://advances.sciencemag.org/content/6/46/eabc2695>.
- 586 27. Fricker, H., Young, N., Allison, I., & Coleman, R. (2002). Iceberg calving from the Amery Ice
587 Shelf, East Antarctica. *Annals of Glaciology*, 34, 241-246. doi:10.3189/172756402781817581

- 588 28. Fricker, H. A., N. W. Young, R. Coleman, J. N. Bassis, and J.-B. Minster (2005), Multi-year
589 monitoring of rift propagation on the Amery Ice Shelf, East Antarctica, *Geophys. Res. Lett.*,
590 32, L02502, doi:10.1029/2004GL021036.
- 591 29. Fogt, RL, Marshall, GJ. The Southern Annular Mode: Variability, trends, and climate impacts
592 across the Southern Hemisphere. *WIREs Clim Change*. 2020; 11:e652.
593 <https://doi.org/10.1002/wcc.652>
- 594 30. Fyfe, J. C. (2003), Extratropical Southern Hemisphere cyclones: Harbingers of climate
595 change?, *J. Clim.*, 16, 2802– 2805.
- 596 31. Galton-Fenzi, B. K., J. R. Hunter, R. Coleman, S. J. Marsland, and R. C. Warner (2012),
597 Modeling the basal melting and marine ice accretion of the Amery Ice Shelf, *J. Geophys. Res.*,
598 117, C09031, doi:10.1029/2012JC008214.
- 599 32. Greenbaum, J., Blankenship, D., Young, D. et al. Ocean access to a cavity beneath Totten
600 Glacier in East Antarctica. *Nature Geosci* 8, 294–298 (2015).
601 <https://doi.org/10.1038/ngeo2388>.
- 602 33. Grieger J., G. C. Leckebusch, C. C. Raible, I. Rudeva & I. Simmonds (2018) Subantarctic
603 cyclones identified by 14 tracking methods, and their role for moisture transports into the
604 continent, *Tellus A: Dynamic Meteorology and Oceanography*, 70:1, 1-18, DOI:
605 10.1080/16000870.2018.1454808.
- 606 34. Hersbach, H., B. Bell, P. Berrisford, et al., 2020: The ERA5 global reanalysis. *Quarterly*
607 *Journal of the Royal Meteorological Society*, 146, 1999–2049, doi: 10.1002/qj.3803. Hogg, A.,
608 Gudmundsson, G. Impacts of the Larsen-C Ice Shelf calving event. *Nature Clim Change* 7,
609 540–542 (2017). <https://doi.org/10.1038/nclimate3359>.
- 610 35. Holdsworth, G. & Glynn, J. Iceberg calving from floating glaciers by a vibration mechanism.
611 *Nature* 274, 464–466 (1978).
- 612 36. Hudson, R. D.: Measurements of the movement of the jet streams at mid-latitudes, in the
613 Northern and Southern Hemispheres, 1979 to 2010, *Atmos. Chem. Phys.*, 12, 7797–7808,
614 <https://doi.org/10.5194/acp-12-7797-2012>, 2012.
- 615 37. Irving, D., & Simmonds, I. (2015). A Novel Approach to Diagnosing Southern Hemisphere
616 Planetary Wave Activity and Its Influence on Regional Climate Variability, *Journal of Climate*,
617 28(23), 9041-9057. Retrieved Jan 28, 2021, from
618 <https://journals.ametsoc.org/view/journals/clim/28/23/jcli-d-15-0287.1.xml>.
- 619 38. Jeong, S., I. M. Howat, and J. N. Bassis (2016), Accelerated ice shelf rifting and retreat at Pine
620 Island Glacier, West Antarctica, *Geophys. Res. Lett.*, 43, 11,720–11,725,
621 doi:10.1002/2016GL071360.
- 622 39. King, M. A., R. Coleman, A.-J. Freemantle, H. A. Fricker, R. S. Hurd, B. Legrésy, L. Padman,
623 and R. Warner (2009), A 4-decade record of elevation change of the Amery Ice Shelf, East
624 Antarctica, *J. Geophys. Res.*, 114, F01010, doi:10.1029/2008JF001094.
- 625 40. Kohout, A., Williams, M., Dean, S. et al. Storm-induced sea-ice breakup and the implications
626 for ice extent. *Nature* 509, 604–607 (2014). <https://doi.org/10.1038/nature13262>
- 627 41.
- 628 42. Kwok, R., Pang, S. S., and Kacimi, S.: Sea ice drift in the Southern Ocean: Regional patterns,
629 variability and trends, *Elem. Sci. Anth.*, 5, 1–16, <https://doi.org/10.1525/elementa.226>, 2017.

- 630 43. Lambert, S. J., and J. C. Fyfe (2006), Changes in winter cyclone frequencies and strengths
631 simulated in enhanced greenhouse warming experiments: Results from the models
632 participating in the IPCC diagnostic exercise, *Clim. Dyn.*, 26, 713–728.
- 633 44. Lavergne, T., Eastwood, S., Teffah, Z., Schyberg, H., and Breivik, L.-A. (2010), Sea ice
634 motion from low-resolution satellite sensors: An alternative method and its validation in the
635 Arctic, *J. Geophys. Res.*, 115, C10032, doi:10.1029/2009JC005958.
- 636 45. Lee, S., Gong, T., Feldstein, S. B., Screen, J. A., & Simmonds, I. (2017). Revisiting the cause
637 of the 1989–2009 Arctic surface warming using the surface energy budget: Downward infrared
638 radiation dominates the surface fluxes. *Geophysical Research Letters*, 44, 10,654–10,661.
639 <https://doi.org/10.1002/2017GL075375>.
- 640 46. Lim, Eun-Pa; Simmonds, Ian (2002). Explosive Cyclone Development in the Southern
641 Hemisphere and a Comparison with Northern Hemisphere Events. *Monthly Weather Review*.
642 130 (9): 2188–2209. Bibcode:2002 MWRv. .130.2188L. doi:10.1175/1520-
643 0493(2002)130<2188:ECDITS>2.0.CO;2.
- 644 47. Liu Y., J. C. Moore, X. Cheng, R. M. Gladstone, J. N. Bassis, H. Liu, J. Wen, F. Hui, 2015,
645 Iceberg calving of Antarctic ice shelves, *Proceedings of the National Academy of Sciences*,
646 March 2015, 112 (11) 3263–3268; DOI: 10.1073/pnas.1415137112.
- 647 48. Mann, M., Rahmstorf, S., Kornhuber, K. et al. Influence of Anthropogenic Climate Change on
648 Planetary Wave Resonance and Extreme Weather Events. *Sci Rep* 7, 45242 (2017).
649 <https://doi.org/10.1038/srep45242>
- 650 49. Massom, R.A., Scambos, T.A., Bennetts, L.G. et al. Antarctic ice shelf disintegration triggered
651 by sea ice loss and ocean swell. *Nature* 558, 383–389 (2018). [https://doi.org/10.1038/s41586-](https://doi.org/10.1038/s41586-018-0212-1)
652 [018-0212-1](https://doi.org/10.1038/s41586-018-0212-1).
- 653 50. Matear, R., O’Kane, T., Risbey, J. et al. Sources of heterogeneous variability and trends in
654 Antarctic sea-ice. *Nat Commun* 6, 8656 (2015). <https://doi.org/10.1038/ncomms9656>.
- 655 51. Meier, W. N., T. Markus, and J. C. Comiso. 2018. AMSR-E/AMSR2 Unified L3 Daily 12.5
656 km Brightness Temperatures, Sea Ice Concentration, Motion & Snow Depth Polar Grids,
657 Version 1. [Antarctica]. Boulder, Colorado USA. NASA National Snow and Ice Data Center
658 Distributed Active Archive Center. doi: <https://doi.org/10.5067/RA1MIJOYPK3P> [10 April
659 2020].
- 660 52. Morrison K.A., A. M. Hogg, M.H. England and P. Spence Warm Circumpolar Deep Water
661 transport toward Antarctica driven by local dense water export in canyons, *Science Advances*,
662 2020: Vol. 6, no. 18, eaav2516, DOI: 10.1126/sciadv.aav2516.
- 663 53. Moustouli, M., H. Teitelbaum, C. Basdevant, and Y. Boughaleb, Linked behavior of twin
664 tropical cyclones, *J. Geophys. Res.*, 107(D19), 4378, doi:10.1029/2000JD000066, 2002.
- 665 54. Neu, U., Akperov, M. G., Bellenbaum, N., Benestad, R., Blender, R., Caballero, R., Coccozza,
666 A., Dacre, H. F., Feng, Y., Fraedrich, K., Grieger, J., Gulev, S., Hanley, J., Hewson, T., Inatsu,
667 M., Keay, K., Kew, S. F., Kindem, I., Leckebusch, G. C., Liberato, M. L. R., Lionello, P.,
668 Mokhov, I. I., Pinto, J. G., Raible, C. C., Reale, M., Rudeva, I., Schuster, M., Simmonds, I.,
669 Sinclair, M., Sprenger, M., Tilinina, N. D., Trigo, I. F., Ulbrich, S., Ulbrich, U., Wang, X. L.,
670 & Wernli, H. (2013). IMILAST: A Community Effort to Intercompare Extratropical Cyclone
671 Detection and Tracking Algorithms, *Bulletin of the American Meteorological Society*, 94(4),

672 529-547. Retrieved Jan 28, 2021, from
673 <https://journals.ametsoc.org/view/journals/bams/94/4/bams-d-11-00154.1.xml>.

674 55. ORNL DAAC. 2018. MODIS and VIIRS Land Products Global Subsetting and Visualization
675 Tool. ORNL DAAC, Oak Ridge, Tennessee, USA. Accessed May 20, 2020. Subset obtained
676 for MOD13Q1 product over the Amery Ice Shelf – Antarctica, time period: 2019-09-01 to
677 2019-09-30. <https://doi.org/10.3334/ORNLDAAC/1379>.

678 56. Pezza, A.B., Simmonds, I. and Renwick, J.A. (2007), Southern hemisphere cyclones and
679 anticyclones: recent trends and links with decadal variability in the Pacific Ocean. *Int. J.*
680 *Climatol.*, 27: 1403-1419. <https://doi.org/10.1002/joc.1477>.

681 57. Pope, J. O., Holland, P. R., Orr, A., Marshall, G. J., and Phillips, T. (2017), The impacts of El
682 Niño on the observed sea ice budget of West Antarctica, *Geophys. Res. Lett.*, 44, 6200– 6208,
683 doi:10.1002/2017GL073414.

684 58. Pritchard, H. D., Ligtenberg S.R., Fricker H.A., Vaughan D.G., van den Broeke MR, Padman
685 L., Antarctic ice-sheet loss driven by basal melting of ice shelves. *Nature* 484, 502–505 (2012).

686 59. Reale M., M. L.R. Liberato, P. Lionello, J. G. Pinto, S. Salon & S. Ulbrich (2019) A Global
687 Climatology of Explosive Cyclones using a Multi-Tracking Approach, *Tellus A: Dynamic*
688 *Meteorology and Oceanography*, 71:1, DOI: 10.1080/16000870.2019.1611340.

689 60. Raphael, M. N., 2007, The influence of atmospheric zonal wave three on Antarctic sea ice
690 variability, *J. Geophys. Res.*, 112, D12112, <https://doi.org/10.1029/2006JD007852>, 2007.

691 61. Renfrew A.I., G.W.K. Moore and A.A. Clerk (1997) Binary interactions between polar lows,
692 *Tellus A: Dynamic Meteorology and Oceanography*, 49:5, 577-594, DOI:
693 10.3402/tellusa.v49i5.14823.

694 62. Rignot, E. et al. Accelerated ice discharge from the Antarctic Peninsula following the collapse
695 of Larsen B ice shelf. *Geophys. Res. Lett.* 31, <https://doi.org/10.1029/2004gl020697> (2004).

696 63. Rignot E., J. Mouginot, B. Scheuchl, M. van den Broeke, M. J. van Wessem, M. Morlighem,
697 2019, Four decades of Antarctic Ice Sheet mass balance from 1979–2017, *Proceedings of the*
698 *National Academy of Sciences* Jan 2019, 116 (4) 1095-1103; DOI: 10.1073/pnas.1812883116.

699 64. Robinson, W. & Haskell, T. G. Calving of Erebus Glacier tongue. *Nature* 346, 615–616 (1990).

700 65. Robinson, W. & Haskell, T. G. Travelling flexural waves in the Erebus Glacier Tongue,
701 McMurdo Sound, Antarctica. *Cold Reg. Sci. Technol.* 20, 289–293 (1992).

702 66. Rudeva I., I. Simmonds, Variability and trends of global atmospheric frontal activity and links
703 with large-scale modes of variability. *J. Climate* 28, 3311–3330 (2015).

704 67. Sanders, Frederick; Gyakum, John R (1980). "Synoptic-Dynamic Climatology of the 'Bomb'".
705 *Monthly Weather Review.* 108 (10): 1589–606. Bibcode:1980 MWRv.108.1589S.
706 doi:10.1175/1520-0493(1980)108<1589:SDCOT>2.0.CO;2.

707 68. Scambos, T. A., Bohlander, J. A., Shuman, C. A. & Skvarca, P. Glacier acceleration and
708 thinning after ice shelf collapse in the Larsen B embayment, Antarctica. *Geophys. Res. Lett.*
709 31,1 –4 (2004).

710 69. Scambos, T., Ross, R., Bauer, R., Yermolin, Y., Skvarca, P., Long, D., Bohlander, J. and
711 Haran, T., 2008. Calving and ice-shelf break-up processes investigated by proxy: Antarctic
712 tabular iceberg evolution during northward drift. *Journal of Glaciology*, 54(187), pp.579-591.

713 70. Scambos, T. A., Berthier, E., Haran, T., Shuman, C. A., Cook, A. J., Ligtenberg, S. R. M., and
714 Bohlander, J.: Detailed ice loss pattern in the northern Antarctic Peninsula: widespread decline

715 driven by ice front retreats, *The Cryosphere*, 8, 2135–2145, [https://doi.org/10.5194/tc-8-2135-](https://doi.org/10.5194/tc-8-2135-2014)
716 2014, 2014.

717 71. Schemm, S. (2018), Regional trends in weather systems help explain Antarctic sea ice trends.
718 *Geophysical Research Letters*, 45, 7165–7175. <https://doi.org/10.1029/2018GL079109>.

719 72. Schlosser E., J.G. Powers, M.G. Duda, K.W. Manning (2011) Interaction between Antarctic
720 sea ice and synoptic activity in the circumpolar trough: implications for ice-core interpretation,
721 *Annals of Glaciology* 52(57) 2011.

722 73. Schlosser E., F. A. Haumann, M. N. Raphael Atmospheric influences on the anomalous 2016
723 Antarctic sea ice decay (2018), *The Cryosphere*, 12, 1103–1119, 2018,
724 <https://doi.org/10.5194/tc-12-1103-2018>.

725 74. Schosler, V., Aquino, F.E., Reis, P.A. et al. Antarctic atmospheric circulation anomalies and
726 explosive cyclogenesis in the spring of 2016. *Theor Appl Climatol* (2020).
727 <https://doi.org/10.1007/s00704-020-03200-9>.

728 75. Shepherd, A., Fricker, H. A. & Farrell, S. L. Trends and connections across the Antarctic
729 cryosphere. *Nature* 558, 223–232 (2018).

730 76. Shimada, U., A. Wada, K. Yamazaki, N. Kitabatake (2014) Roles of an upper-level cold vortex
731 and low-level baroclinicity in the development of polar lows over the Sea of Japan, *Tellus A:*
732 *Dynamic Meteorology and Oceanography*, 66:1, DOI: 10.3402/tellusa.v66.24694.

733 77. Smith, J.A., Graham, A.G.C., Post, A.L. et al. The marine geological imprint of Antarctic ice
734 shelves. *Nat Commun* 10, 5635 (2019). <https://doi.org/10.1038/s41467-019-13496-5>.

735 78. Son, S.-W., L. M. Polvani, D. W. Waugh, H. Akiyoshi, R. Garcia, D. Kinnison, S. Pawson, E.
736 Rozanov, T. G. Shepherd, and K. Shibata (2008), The impact of stratospheric ozone recovery
737 on the Southern Hemisphere westerly jet, *Science*, 320, 1486– 1489.

738 79. Squire, V. A., Robinson, W. H., Meylan, M. H. & Haskell, T. G. Observations of flexural
739 waves in the Erebus Glacier Tongue, McMurdo Sound, Antarctica, and nearby sea ice. *J.*
740 *Glaciol.* 40, 377–385 (1994).

741 80. Stoll P.J., Graverson RG., Noer G, Hodges K. An objective global climatology of polar lows
742 based on reanalysis data. *QJRMeteorol.Soc.*2018;144:2099–2117.
743 <https://doi.org/10.1002/qj.3309>

744 81. Swart S., E. C. Cambell, C. H. Heuze, K. Johnson, J. L. Lieser, R. Masson, M. Mazloff, M.
745 Meredith, P. Reid, J.-B. Sallee, S. Stammerjohn (2018) Litmus or sea ice anomaly? Sidebar,
746 *State of the Climate, BAMS*, August 2018, DOI:10.1175/BAMS-D-18-0173.1.

747 82. Tamarin, T., and Y. Kaspi (2017), The poleward shift of storm tracks under global warming:
748 A Lagrangian perspective, *Geophys. Res. Lett.*, 44, 10,666–10,674,
749 doi:10.1002/2017GL073633.

750 83. Li T., Y. Liu and X. Cheng, 2020: Recent and imminent calving events do little to impair
751 Amery ice shelf's stability. *Acta Oceanologica Sinica*, 39, 168-170, doi: 10.1007/s13131-020-
752 1600-6.

753 84. Turner J., S.A. Harangozo, G.J. Marshall, J.C. King, S.R. Colwell (2002) Anomalous
754 atmospheric circulation over the Weddell Sea, Antarctica during the Austral summer of
755 2001/02 resulting in extreme sea ice conditions, *Geophys.Res. Lett.*, Vol. 29, N0. 24, 2160,
756 doi:10.1029/2002GL015565, 2002.

- 757 85. Uccellini L.W. (1990) Processes Contributing to the Rapid Development of Extratropical
758 Cyclones. In: Newton C.W., Holopainen E.O. (eds) Extratropical Cyclones. American
759 Meteorological Society, Boston, MA.
- 760 86. Ulbrich, U., Leckebusch, G. C., Grieger, J., Schuster, M., Akperov, M., Bardin, M. Y., Feng,
761 Y., Gulev, S., Inatsu, M., Keay, K., Kew, S. F., Liberato, M. L. R., Lionello, P., Mokhov, I. I.,
762 Neu, U., Pinto, J. G., Raible, C. C., Reale, M., Rudeva, I., Simmonds, I., Tilinina, N. D., Trigo,
763 I. F., Ulbrich, S., Wang, X. L. and Wernli, H. (2013) Are greenhouse gas signals of Northern
764 Hemisphere winter extra-tropical cyclone activity dependent on the identification and tracking
765 algorithm? *Meteorologische Zeitschrift*, 22 (1). pp. 61-68. ISSN 0941-2948. doi:
766 <https://doi.org/10.1127/0941-2948/2013/0420>.
- 767 87. Uotila, P., T. Vihma, A. B. Pezza, I. Simmonds, K. Keay, and A. H. Lynch (2011),
768 Relationships between Antarctic cyclones and surface conditions as derived from high-
769 resolution numerical weather prediction data, *J. Geophys. Res.*, 116, D07109,
770 doi:10.1029/2010JD015358.
- 771 88. Vaughan, D. G., H. F. J. Corr, R. A. Bindschadler, P. Dutrieux, G. H. Gudmundsson, A.
772 Jenkins, T. Newman, P. Vornberger, and D. J. Wingham (2012), Subglacial melt channels and
773 fracture in the floating part of Pine Island Glacier, Antarctica, *J. Geophys. Res.*, 117, F03012,
774 doi:10.1029/2012JF002360.
- 775 89. Vernon A. Squire, 2020: Ocean wave interactions with sea ice: A reappraisal. *Annual Review*
776 *of Fluid Mechanics*, 52, 37-60, doi: 10.1146/annurev-fluid-010719-060301.
- 777 90. Vichi, M., Eayrs, C., Alberello, A., Bekker, A., Bennetts, L., Holland, D., et al. (2019). Effects
778 of an explosive polar cyclone crossing the Antarctic marginal ice zone. *Geophysical Research*
779 *Letters*, 46, 5948–5958. <https://doi.org/10.1029/2019GL082457>.
- 780 91. Wagner J.S., A. Gohm, A. Dörnbrack, A. Schäfler (2011), The mesoscale structure of a polar
781 low: airborne lidar measurements and simulations. *Q. J. R. Meteorol. Soc.* DOI:
782 10.1002/qj.857.
- 783 92. Watanabe, S. I., and H. Niino, 2014: Genesis and Development Mechanisms of a Polar
784 Mesocyclone over the Japan Sea. *Mon. Wea. Rev.*, 142, 2248–2270,
785 <https://doi.org/10.1175/MWR-D-13-00226.1>.
- 786 93. Wei, L., Qin, T. Characteristics of cyclone climatology and variability in the Southern Ocean.
787 *Acta Oceanol. Sin.* 35, 59–67 (2016). <https://doi.org/10.1007/s13131-016-0913-y>.
- 788 94. Wille, J. D., V. Favier, A. Dufour, I. V. Gorodetskaya, J. Turner, C. Agosta and F. Codron,
789 2019: West Antarctic surface melt triggered by atmospheric rivers. *Nature Geoscience*, 12,
790 911-916, doi: 10.1038/s41561-019-0460-1.
- 791 95. Woods, C., and R. Caballero, 2016: The Role of Moist Intrusions in Winter Arctic Warming
792 and Sea Ice Decline. *J. Climate*, 29, 4473–4485, <https://doi.org/10.1175/JCLI-D-15-0773.1>.
- 793 96. Yokoyama, Y.; Yamamoto, M., 2019, Influences of surface heat flux on twin cyclone structure
794 during their explosive development over the East Asian marginal seas on 23 January 2008.
795 *Weather Clim. Extrem.* 2019, 23, 100198. <https://doi.org/10.1016/j.wace.2019.100198>.
- 796 97. Zhao, C., Cheng, X., Liu, Y., Hui, F., Kang, J., Wang, X., Cheng, C. (2013). The slow-growing
797 tooth of the Amery Ice Shelf from 2004 to 2012. *Journal of Glaciology*, 59(215), 592-596.
798 doi:10.3189/2013JoG12J225.